Tidal Interaction of M32 and NGC 205 with M31: Surface Photometry and Numerical Simulations[1]

Philip I. Choi, Puragra Guhathakurta

UCO/Lick Observatory, University of California, Santa Cruz, CA 95064

E-mail: pchoi@ucolick.org, raja@ucolick.org

Kathryn V. Johnston

Van Vleck Observatory, Wesleyan University, Middletown, CT 06459

E-mail: kvj@astro.wesleyan.edu

ABSTRACT

We investigate the interaction history of the M31 sub-group by comparing surface photometry of two of its satellites, M32 and NGC 205, with N-body simulations of satellite destruction. The recent discovery of a giant stream in the outer halo of M31, apparently pointed in the direction of M32 and NGC 205, makes such an investigation particularly relevant. The observational component of this study is based on $1.7° \times 5°$ B- and I-band CCD mosaic images centered on M31 and covering both satellites. Standard ellipse-fitting techniques are used to model and remove M31 disk light and to perform surface photometry on the satellites to limiting brightness levels of $[\mu_B, \ \mu_I] = [27, \ 25]$ mag arcsec^{-2}, corresponding to isophotal semi-major axis lengths of $r_{\lim}^{\rm M32} = 420''$ (1.6 kpc) and $r_{\lim}^{\rm NGC\,205} = 720''$ (2.7 kpc). A hint of excess light in the outer parts of M32 noted in earlier studies is confirmed; in particular, clear evidence is seen for a sharp (upward) break in the surface brightness profile at $r = 150''$ relative to a $r^{1/4}$ law that fits the inner region of M32. This break is accompanied by a steep increase in isophotal ellipticity ϵ as well as position angle ϕ' twisting. In addition to this excess, evidence is seen for an inner downward break in the surface brightness profile at $r = 50''$. The robustness of the M32 isophotal features is demonstrated through their: (1) insensitivity to the details of background subtraction; (2) symmetry about M32's center; and (3) narrow range of $B - I$ color that is consistent with the interior regions of M32 but not with M31 residual spiral arm/dust lane features. The study of NGC 205 reveals pronounced isophote twisting at $r \sim 300''$ that is coincident with a subtle downward break in the surface brightness profile, relative to an exponential law fit to the inner region.

The simulation component of this project is based on the analysis of single-component, spherical satellites that are being tidally disrupted through interactions with their parent galaxy. Generic features of the simulations include an excess in the surface brightness profile at large radii, a depletion zone at intermediate radii, and isophotal elongation and twists that are coincident with breaks in the brightness profile. The two satellites, M32 and NGC 205, display most of these features consistently

across the B and I bands, strongly suggestive of tidal interaction and probable stripping by M31. We discuss what these observed features can tell us about the satellites' orbital parameters and histories. Specifically, M32 is found to be on a highly eccentric orbit and away from pericenter. Investigating M32's unusual combination of high surface brightness and low luminosity (the hallmark of compact ellipticals), we make empirical estimates of the galaxy's intrinsic properties and conclude that it is not likely to be the residual core of a tidally-stripped normal elliptical galaxy as has been suggested, but rather that its precursor was intrinsically compact.

Subject headings: galaxies: dwarf — galaxies: interactions — galaxies: Local Group — galaxies: evolution — galaxies: photometry — galaxies: individual (NGC 205, M32)

1.   Introduction

Globular clusters and satellite galaxies serve as convenient tracers of the mass distribution of their parent galaxy. In theory, even a few well-determined satellite orbits can be used to constrain the gravitational potential field of the central galaxy (Evans et al. 2000). Unfortunately, direct measurement of orbital parameters — the proper motion, in particular — is difficult. It has long been believed that observable signatures of tidal interaction in the satellites can be used to determine at least some of these critical parameters. For instance, it was proposed that globular cluster profiles are limited by the Galactic tidal field in which they are embedded (von Hoerner 1957) and that the anomalous properties of some peculiar elliptical (E) galaxies could be the result of similar tidal interactions (King 1962; Aguilar & White 1986). Since that time, there have been numerous investigations into the dynamics of tidally-truncated systems. Objects such as globular clusters and compact elliptical (cE) galaxies, of which M32 is a prototype, have been modeled with the King modification of the von Hoerner tidal radius formula:

$$r_{\text{tide, peri}} = R_{\text{peri}} \left[\frac{m_{\text{sat}}}{M_{\text{gal, peri}}(e_{\text{orb}} + 3)} \right]^{1/3} \tag{1}$$

where $r_{\text{tide, peri}}$ is the tidal radius of the satellite set at pericenter; R_{peri} is the satellite's pericenter distance; m_{sat} and $M_{\text{gal, peri}}$ are the mass of the satellite galaxy and the mass of the parent galaxy enclosed within the satellite's orbit, respectively; and e_{orb} is the satellite's orbital eccentricity.

Several studies have been based on the assumption that the limiting radius of a truncated object corresponds to its tidal radius at pericenter. Faber (1973) derived perigalacticon distances

---

for a sample of cE galaxies. This was followed by more ambitious attempts to constrain the orbital parameters of Galactic globular clusters (Peterson 1974; Innanen, Harris, & Webbink 1983) and M31 satellite galaxies (Cepa & Beckman 1988). These interpretations provided a qualitative picture of the interactions; however, uncertainties in the determination of the tidal radius prevented the accurate recovery of orbital parameters. In addition, the discovery of extra-tidal stars around Galactic globular clusters (Grillmair et al. 1995) and dwarf spheroidals (Irwin & Hatzidimitriou 1995; Kuhn, Smith, & Hawley 1996) complicated the notion of a well-defined, observable tidal radius. In response to these findings, a slew of detailed numerical simulations emerged that modeled extra-tidal features as well as extended tidal tails (Oh, Lin, & Aarseth 1995; Moore 1996; Combes, Leon, & Meylan 1999; Johnston, Sigurdsson, & Hernquist 1999a). In turn, these motivated further observational studies to more precisely characterize both of these peripheral populations (Majewski et al. 2000; Leon, Meylan, & Combes 2000). Comparisons between observations and models are proving to be powerful tools for probing the Galactic potential (Johnston et al. 1999b) and determining satellite dark matter fractions, mass-loss rates (Johnston et al. 1999a), and orbital parameters.

The proximity of Galactic satellites makes detailed observations possible but we are more or less limited to viewing them from within the plane of their orbit. External systems, while observationally more challenging, offer the advantage of a global perspective on the parent galaxy and a bird's-eye view of the satellites' orbits. Our nearest large galaxy neighbor, the Andromeda spiral (M31), has been the subject of such studies for the last few decades (Byrd 1979; Sato & Sawa 1986). Galaxy interactions in the M31 subgroup have recently been in the limelight due to the discovery of a tidal stream in the outer halo of M31 (Ibata et al. 2001) and hints of tidal debris around its dwarf spheroidal satellites (Ostheimer et al. 2002). In this paper, we investigate signatures of tidal interaction in the outskirts of the luminous M31 satellites, M32 and NGC 205. This is especially relevant since the Ibata et al. stream lies, at least in projection, along a line intersecting both M32 and NGC 205. Our study uses traditional integrated surface photometry techniques in contrast to the star count analyses of Ibata et al. and Ostheimer et al.. Studies of satellite interactions well beyond the Local Group will, into the foreseeable future, likely be restricted to the use of surface photometry methods on relatively high surface brightness, luminous satellites; thus, our work on M32 and NGC 205 may be viewed as a pilot study for more distant systems.

In addition to probing the parent galaxy potential, it is interesting to investigate the impact of tidal interactions on the morphology and evolution of low-mass satellites. The satellites M32 and NGC 205 represent two distinct classes of low-mass galaxies, cEs and dwarf ellipticals (dEs), respectively. Normal E galaxies are found to populate a region in luminosity (L), surface brightness (μ), and internal velocity dispersion (σ) space called the Fundamental Plane (FP). In the μ-L projection of this space, the E galaxy population fainter than $M_B \sim -18$ bifurcates into tracks of (1) high surface brightness, high-metallicity cEs and (2) low surface brightness, low-metallicity dEs (Kormendy 1985). There is no clear formation scenario unifying these three classes of galaxies, and

there has been a long-standing debate about whether cEs or dEs represent the natural low-mass extension of normal Es (Faber 1973; Wirth & Gallagher 1984; Nieto & Prugniel 1987; Bender & Nieto 1990; Kormendy & Djorgovski 1989).

As a class, cE galaxies have de Vaucouleurs law μ profiles like normal Es. Furthermore, they occupy a region of structural parameter space that is the direct low-luminosity extrapolation of the E galaxy fundamental plane (Wirth & Gallagher 1984; Nieto & Prugniel 1987), though well separated from it. On the other hand, the general proximity of cEs to massive parent galaxies has led to speculation that cEs are formed through the capture and tidal truncation of satellite galaxies (King & Kiser 1973; Tonry 1984, 1987). The range of proposed cE progenitors includes Es (Faber 1973), S0s (Nieto 1990), and spirals (Bekki et al. 2001). Alternatively, Burkert (1994a) has proposed a model in which cEs are formed through a starburst and subsequent violent collapse within the potential well of a massive galaxy. If cEs are the low-mass counterparts of normal Es, their rarity (Ziegler & Bender 1998; Drinkwater & Gregg 1998) and small range of absolute magnitudes would imply a sharp turnover in the E galaxy mass function.

By contrast, dEs tend to: (1) be fit by a King or exponential μ profile instead of a de Vaucouleurs law and (2) form a track in μ-L space that is perpendicular to the classical E galaxy track. Such structural differences do not however rule out the possibility of a connection between dE and E galaxies since different physical processes may be at work in high versus low mass galaxies. The conventional wisdom regarding dE formation has been that, given their low binding energies, they are susceptible to supernova-driven galactic winds that regulate star formation, expand the stellar component, and thereby produce diffuse density profiles (Burkert 1994b and references therein). Recent simulations have contested these claims and suggested that mechanisms such as galaxy harassment (Moore et al. 1996; Moore, Lake, & Katz 1998; Moore et al. 1999) and tidal heating (Mayer et al. 2001a,b) may be responsible for the transformation of spiral and dwarf irregular galaxies into dEs. Far more numerous than cEs, dEs populate an wide range of absolute magnitudes fainter than $M_B \sim -18.0$, beyond the sharp faint-end cutoff of the cE luminosity function. If dEs are the low-mass counterparts of normal Es, it would imply that the low end of the E galaxy mass function has a smooth extension.

Tidal interactions may also have some bearing on M32's unusual stellar content. Its stellar mix has been a controversial topic, with suggestions ranging from a pure old population (Cole et al. 1998) to a single coeval intermediate-age population (Vazdekis & Arimoto 1999; del Burgo et al. 2001). More plausibly, M32 seems to contain a small fraction of intermediate-age stars mixed in with an underlying old population (O'Connell 1980; Burstein et al. 1984; Rose 1985; Bica, Alloin, & Schmidt 1990; Davidge et al. 2000). Proposed theories for the origin of this secondary stellar population invoke galaxy interactions as a trigger for star formation within M32 or in the context of accretion of gaseous material.

The M31 satellites M32 and NGC 205 are thus good test subjects for investigating the formation and evolution of these two classes of low-mass early-type galaxies. In this paper, a large-format

CCD mosaic image is used to carry out surface photometry of the satellites. Earlier studies of these systems have been plagued by large uncertainties in the measurement of their faint outer isophotes: photographic studies (de Vaucouleurs 1953; Hodge 1973) are hampered by low-level plate-fog variations, while more recent CCD observations (Kent 1987; Peletier 1993) have limited fields of view making sky subtraction problematic. The situation is complicated by the fact that the satellites' outer brightness profiles are contaminated by M31 disk light. The large field of view of our CCD mosaic image makes global modeling and subtraction of M31's disk light possible, thereby allowing for reliable measurement of the satellites' faint isophotes. These measurements are compared to numerical simulations to place constraints on the orbital parameters and mass-loss rates of the satellites and to estimate the evolution of M32's luminosity and central surface brightness.

This paper is divided into the following sections. A summary of the observations and an overview of the basic data reduction procedure are given in §2. The removal of "background" M31 light is discussed in §3. Details of the surface photometry of M32 and NGC 205 are presented in §4 and §5, respectively. A comparison of the observations to numerical simulations is presented in §6, and implications for the evolution of M32 are discussed in §7. The main points of the paper are summarized in §8.

2. Observations and Basic Data Processing

The observations were carried out over the course of four nights in 1992 October/November using the Kitt Peak National Observatory 0.9/0.6-m (primary mirror/corrector) Burrell Schmidt telescope with a Tektronix ST2KA 2048×2048 CCD. Each CCD frame has a field of view of $68' \times 68'$ and is slightly vignetted at the corners. The pixel scale is $2\rlap{.}''03$ and the typical FWHM of stellar images is in the range of 2–5 pixels ($4'' - 10''$) due to seeing and, in the worst cases, poor focus. The data set consists of 22×10-min exposures in the B band and 35×10-min exposures in the I band.

After overscan/bias subtraction, trimming, and flat-fielding, each individual CCD frame is geometrically transformed onto a distortion-free astrometric system defined by the HST Guide Star Catalog. The images in each band are then flux calibrated to a common photometric system, corrected for temporal variations in the night-sky brightness, and mosaiced into a composite image. The reader is referred to Guhathakurta, Choi, & Raychaudhury (2002) for the details of the mosaicing technique and least-squares method of transparency and sky-brightness corrections.

The final B- and I-band mosaic images each cover a $\sim 1.7° \times 5°$ region centered on M31. Though both mosaics cover all of M32, only the B-band mosaic covers all of NGC 205. The I-band coverage is limited to the SE half of the galaxy. Due to varying degrees of frame overlap, the effective exposure time is not uniform across the entire field of view; typical effective exposure times are 20 min in B and 40 min in I.

3. Removal of M31's Disk Light

The projected distance between M31 and its two nearest satellites is small enough that there is significant overlap in their light distributions. At the location of M32's center, for example, M31's disk light accounts for $\sim$12% of the background in both B and I bands. In addition, its steeply sloped contribution varies from $\sim$5% $-$ 20% between M32's SE and NW extremities ($r = 300''$). An investigation of the satellites' global properties requires a careful treatment of this contamination. Previous attempts to remove the M31 light contribution from the satellite profiles have relied on a simple plane or a low-order polynomial fit to the *local* background (Kent 1987; Peletier 1993). While this approach is successful in modeling the smooth contribution of M31's disk, it is not as effective at removing disk features such as spiral arms. The advantage of using a large-format CCD mosaic image is that it allows for the *global* modeling and subtraction of M31's disk light.

For the purpose of modeling the M31 disk only, the original B- and I-band CCD mosaic images are median-filtered using a $30'' \times 30''$ window. The resulting image is largely free of foreground Galactic stars and compact M31 disk features. The implementation of a two-dimensional exponential disk plus de Vaucouleurs bulge model reveals strong departures from global symmetry in the form of large-scale disk warps and spiral arms. By contrast, the more empirical approach of modeling M31 annulus by annulus with elliptical isophotes better reproduces its global light distribution: it provides enough flexibility to fit large- and intermediate-scale structures on scales larger than the angular extent of the two satellites. A series of ellipses is fit to the M31 disk isophotes by applying the IRAF/STSDAS task ELLIPSE to the star-removed, median-filtered images in each of the B and I bands. Figure 1 shows only the best-fit ellipses in the semi-major axis range $30' < r < 70'$ overlaid on the original (i.e., unfiltered) B-band CCD mosaic image; the *full* M31 fit extends to a semi-major axis length $r = 138'$ and even overlaps with NGC 205. Compared to previous attempts to remove M31's disk light, the ellipse-based coordinate system is a more natural choice for modeling the spiral arm structure which is often sharp in the radial dimension, but extended in the azimuthal dimension. The best-fit ellipse models are subtracted from the original mosaic images to create residual images containing the satellites, largely free of M31 disk light. Figure 2 shows B-band images of M32, before and after M31 subtraction, emphasizing the importance of careful subtraction. Though the majority of M31's disk light is well-subtracted in the latter image, fine-scale residual structure such as dust lanes and star-forming knots in the spiral arms are still evident. This residual fine-scale structure is a potential source of systematic error in the surface photometry of M32's faint outer regions (see §4.4).

4. M32

Due to its small projected separation of only 5.5 kpc from the large spiral galaxy M31, M32 is a good test case for investigating tidal effects on satellite galaxies. The high surface brightness inner isophotes of M32 are nearly circular and are well characterized by an $r^{1/4}$ law μ profile.

The inner brightness distribution provides a rather simple (extrapolated) baseline with respect to which subtle departures in the outer parts might be identified and measured. These include sharp features or "breaks" in the μ profile, isophotal elongation and twists, and other signatures of tidal interaction. As discussed in §1 above, such a study is relevant because: (1) M32 is the prototype of the rare class of cE galaxies that may result from the tidal truncation of normal E galaxies, (2) its proximity allows for detailed observations that are currently unavailable for any other object in its class, and (3) the recently discovered stream in the outer halo of M31 (Ibata et al. 2001) might be tidal debris from M32 or NGC 205.

A complicating factor in the study of M32 is the fact that it happens to be superposed onto the face of M31. Figure 3 shows M32 at two contrast levels in each of the I and B bands. The high-contrast panels on the right reveal that a significant amount of fine-scale residual structure remains even after our best attempts to model and subtract M31's disk light. This fine-scale structure is most prominent in the B band on the NW side of the M32 nucleus, toward the bright inner disk of M31; it is probably associated with dust lanes and star-forming regions. In §4.4, tests are carried out to characterize the effect of these residual contaminating M31 disk features on measurements of the faint outer isophotes of M32.

4.1.   Surface Brightness Profile

Surface photometry is carried out using standard ellipse-fitting techniques with the IRAF task ELLIPSE, independently in B and I bands. Measurements are made out to a semi-major axis length of $r \sim 425''$ (1.6 kpc), which corresponds to a limiting surface brightness level of $[\mu_B,\ \mu_I] = [27,\ 25]$ mag arcsec^{-2}. Ellipse fits are performed in three ways: on the entire galaxy, on the NW half only, and on the SE half only. Unless otherwise noted, the measurements of M32's surface brightness (μ), isophotal ellipticity (ϵ), and isophotal position angle (ϕ or ϕ')[2] presented in the rest of this paper are based on ellipse fits to M32's SE half, as it is least susceptible to contamination from M31's inner disk; the global and NW-half ellipse fits are only used to test the symmetry of M32's isophotes (§4.4.1). The central positions of the fitted ellipses are held fixed at the nominal value determined from the innermost isophotes (the obvious nucleus of M32), while their ϵ and ϕ' are allowed to vary with semi-major axis from ellipse to ellipse. The best-fit ellipses with semi-major axis length $100'' < r < 300''$ are overlaid on the B- and I-band M32 images in Figure 3, illustrating the radial extent of the low surface brightness region.

Radial profiles of μ, ϵ, and ϕ', derived from the best-fit elliptical isophotes, are presented in

---

[2]The position angle ϕ is defined following the usual observational convention: anticlockwise from N (i.e., N through E). For the numerical simulations, however, the position angle (ϕ in Paper I) is defined with respect to the satellite→parent line increasing towards the satellite's projected direction of motion, this being the natural coordinate system for the simulations. By analogy, we define the quantity, $\phi'_{\rm M32} = \pm(\phi_{\rm M32} - 1.1°)$, where the positive sign is adopted corresponding to a clockwise projected orbit for M32 around M31 (§§ 6.3–6.4).

Figure 4 in $r^{1/4}$ (left) and log-linear coordinates (right). The B- and I- band profiles are all seen to be in good agreement with each other. A comparison to the R-band study of Kent (1987), shows that the μ profiles are consistent out to his limiting measured isophote of $r \sim 300''$. By contrast the ϵ and ϕ' profiles are consistent only out to $r \sim 200''$; beyond this radius, these isophotal shape parameters are frozen in Kent's study at their last fit values due to insufficient signal-to-noise. Figure 5a shows an I-band image of M32, in contrast to an M32 residual image (Fig. 5b), in which the best-fit ellipse model for M32 has been subtracted. The smoothness of the latter residual image provides a measure, albeit qualitative, of the goodness of the M32 ellipse fits.

A de Vaucouleurs $r^{1/4}$ law profile is a convenient way to parameterize M32's radial μ distribution. Independent fits to the B- and I-band data, over a 5.5 mag range in μ from $10'' < r < 140''$, yield best-fit $r^{1/4}$ law profiles with $r_{B,I}^{\mathrm{eff}} = 29''$, $\mu_I^{\mathrm{eff}} = 17.53$ mag arcsec^{-2}, and $\mu_B^{\mathrm{eff}} = 19.43$ mag arcsec^{-2}. This "standard" fit is in general agreement with Kent's R-band fit over the semi-major axis range $15'' < r < 100''$: $r_R^{\mathrm{eff}} = 32''$ and $\mu_R^{\mathrm{eff}} = 18.79$ mag arcsec^{-2}. While there is excellent overall consistency across BRI bands, close inspection reveals systematic differences between this "standard" $r^{1/4}$ law fit and M32's actual μ profile. These differences, as well as alternative $r^{1/4}$ law fits, will be explored further in §4.3; for the sake of comparison to previous analyses, the "standard" $r^{1/4}$ law fit is adopted in the following section.

4.2. A de Vaucouleurs Profile Excess: The "Faint Diffuse Plume" Revisited

From Figure 3 it is clear that although M32 appears truncated and predominantly spherical in low-contrast images, it is surrounded by a skirt of low surface brightness material that becomes increasingly elongated at large radii. This was originally detected in photographs as a "faint diffuse plume curved away from M31's disk" by Arp (1966), and later described by Kent (1987) as "an excess of light at large radii." Detailed characterization of this region, however, has proven to be elusive until now. The onset of this "faint diffuse plume" in the μ profile of Figure 4 is marked by a clear *upward* break at $r \sim 150''$ with respect to the "standard" $r^{1/4}$ law profile. The excess is coincident with sharp shifts in ϵ and ϕ' in both B and I bands, and is measurable to $r > 300''$ with a peak departure of $\Delta\mu = 0.5$ mag above the extrapolation of the "standard" fit. The semi-major axis range of the isophotes plotted in Figure 3 ($100'' < r < 300''$) is marked with a double line in the top panel of Figure 4 in order to illustrate the region over which the excess is found. Inspecting the relevant portion of the image (Fig. 3), it is clear why this excess feature was previously classified by Arp as a "diffuse plume." In early photographic studies, which were sensitive to blue light, the excess region was swamped by M31's disk structure on the NW side of M32, leading to a one-sided detection. Coupled with sharp changes in ϵ and ϕ' (Fig. 4), the excess appeared to be an asymmetric and disjoint feature alongside an otherwise well-behaved E galaxy.

Uncertainties in the surface photometry of the M32 outskirts are dominated by systematic errors that are difficult to quantify. Our finding of sudden elongations and twists in the ϵ and ϕ' profiles, at radii coincident with the excess in the μ profile, indirectly indicates that our measure-

ments are reliable. This is in contrast to the Kent (1987) study: although Kent's μ_R measurements are in general agreement with ours, the undetermined values for ϵ and ϕ' beyond $r \gtrsim 200''$ in his study made it difficult, at the time, to draw any firm conclusions about the low surface brightness features in M32.

Figure 4 also reveals a previously undetected feature in the form of a subtle downturn in the μ profile at $r \sim 250''$. Although this is near the reliability limit of our data, it is seen in both colors and is accompanied by another isophote twist in ϕ', as well as a flattening in the ϵ profile.

A note of caution may be in order here. Ellipse parameters ϕ', ϵ, and, to a lesser extent, μ are all coupled, so the mere coincidence of the profile features does not eliminate the possibility that they are the result of an M31 disk residual or an asymmetric feature in M32. This possibility can, however, be ruled out via additional tests of the background subtraction and isophotal symmetry and color; these tests will be discussed in §4.4.

4.3. Evidence for an Inner Break and Depletion Zone

Decoupling M32's tidal interaction features from its intrinsic profile requires some a priori assumptions about its unperturbed properties. The "standard" $r^{1/4}$ law fit is a good global fit to M32's current μ profile; however, if tidal interactions have affected its outer isophotes, alternative fits that are limited to M32's inner regions should be more representative of its intrinsic profile.

In the left panels of Figure 6, the μ profile is plotted with the "standard" fit overlaid (top) along with the $\Delta\mu$ residuals of this fit (bottom). Systematic differences are seen between the measured profile and this best-fit $r^{1/4}$ law. Within the radius range $10'' < r < 140''$ (indicated by double lines) over which the $r^{1/4}$ law is fit, these departures correspond to at least one and possibly two additional μ profile breaks.

In the middle and right panels, the same μ profiles are shown with "inner" and "extreme-inner" $r^{1/4}$ laws that are fit to more restricted radius ranges of $10'' < r < 65''$ and $10'' < r < 30''$, respectively. These alternative profiles are shallower than the "standard" fit, have larger values of r_{eff} ($r^{\text{eff}}_{\text{inner}} \sim 37''$ and $r^{\text{eff}}_{\text{extreme-inner}} \sim 44''$) and fainter effective surface brightnesses. Table 1 summarizes the parameters of the different $r^{1/4}$ law fits in the different bands: the radial range over which the data are fit, r_{eff}, and μ_{eff}.

These alternative $r^{1/4}$ law fits bring a new feature to light in M32. In addition to the upward break at $r \sim 150''$ and its associated excess region at large radii, there is evidence for an inner radius *downward* break at $r \sim 50''$ and a "depletion zone" in which the surface brightness is diminished with respect to the extrapolated $r^{1/4}$ law profile. Though the measured μ profile is the same in each panel, its interpretation depends on which $r^{1/4}$ law is adopted as the intrinsic profile. For instance, going from the "standard" to the "extreme-inner" fit, the residuals exhibit the general trend of a de Vaucouleurs law profile with an excess region at large radii to one with an increasingly

significant depletion zone at intermediate radii. In particular, a downward break in the μ profile can be clearly identified in the last two residual plots at $r \sim 50''$. This previously unrecognized break is coincident with an inner twist in the ϕ' profile, supporting the theory that they have a common, presumably tidal, origin.

To verify the significance of the departures discussed above, the two-dimensional surface brightness distribution of M32 is studied. Residual images shown in Figure 7b–d are generated by subtracting a de Vaucouleurs law model of M32's light distribution from the original M32 image. The models are based on the "standard", "inner" and "extreme-inner" $r^{1/4}$ law fits and the measured ϵ and ϕ' ellipse-fit profiles. In each panel, a pair of concentric circles mark the inner and outer radius limits of the associated $r^{1/4}$ law fit. As a contrast, the residual image of M32's *actual* μ profile is shown in Figure 7a (same as Fig. 5b), with all of the aforementioned radius limits overlaid.

The images in Figure 7 reveal that the departures from the various $r^{1/4}$ law profile fits are not only systematic in radius, as illustrated in the Figure 6 plots, but also azimuthally symmetric. The systematic nature of the residuals indicate that they cannot be simply reconciled with localized features like star formation regions. This global symmetry also reaffirms the investigation of the alternative $r^{1/4}$ law profile fits. Going from the "standard" to "extreme-inner" fit, the trend to a more prominent depletion zone and a less prominent excess region, seen in the azimuthally averaged residual profiles, is clearly evident in the images as well.

A priori, there is little reason to assume that one de Vaucouleurs law fit is more representative of the intrinsic profile than any other; however, as will be seen in §6, the simulations provide some useful hints. They indicate that generic profiles of interacting satellites all show evidence of depletion and excess regions. This implies that the interpretation of M32 based on the "inner" and "extreme-inner" fits may be the most physically significant. The implications for the evolution and tidal interaction history of M32 will be addressed in §7.

4.4. Testing the Robustness of the Measured Brightness Distribution

Comparison of the observations to N-body simulations hinges on the reliability of the quantities derived from the isophote fits. It is critical to test for potential systematic errors that may bias the photometry. Two approaches are taken to convince ourselves and the reader that the measured faint features in the M32 outskirts are not artifacts of the reduction procedure or M31 contamination. The first is an investigation of background subtraction errors and isophote symmetry. The second is a color test of M32's extended isophotes. Discussions of these are presented below.

4.4.1. Background Subtraction and Symmetry

Accurate measurement of low surface brightness, extended isophotes requires a careful characterization of the sky and spatially variable M31 contribution. In order to verify that features such as the upward break in the depletion zone ($r \sim 150''$) are not relics of the reduction, the robustness of M32's μ, ϵ, and ϕ' profiles against various background errors is tested. The B- and I-band $\Delta\mu$ plots in Figure 8 and the ϵ and ϕ' plots in Figure 9 illustrate the results of these tests.

The primary concern regarding the measurement of M32's outer isophotes is the accurate removal of M31's disk contribution. The ideal M31 disk fit minimizes residuals in the regions around M32, and not necessarily over M31's entire disk. A simple global model allows for the fitting of large-scale background features; however, it also introduces the problem that asymmetries in the disk can produce a biased subtraction near M32. A range of different rejection thresholds and weighting functions for the M31 fit are tested to minimize the impact of such asymmetries. Ultimately, the best fit is based on the visual inspection of the background after M31 subtraction. In Figure 8a, the M32 $r^{1/4}$ law residuals, based on the "inner" de Vaucouleurs law, are compared for three images with different M31 subtractions. The best-fit M31 subtraction is adopted in one (Case A: triangles) while an under-subtraction (Case B: squares) and an over-subtraction (Case C: circles) of M31 features in the vicinity of M32 are adopted in the others. It is interesting to note that it is only beyond $r \sim 250''$ that the residuals start to diverge. This illustrates the robustness of the surface photometry over the depletion zone and excess region. The ϵ and ϕ' profiles for the different M31 subtractions, shown in Figure 9a and Figure 9c, are also seen to be fairly insensitive to the M31 subtraction in both the B and I band. For the remaining de Vaucouleurs law residual plots, the best-fit M31 subtraction is adopted.

The second concern is the careful treatment of M31's residuals around M32, after the best-fit M31 subtraction has been performed. Although the M32 isophote fit allows for the spatial filtering of background sources, it is difficult to filter non-uniform variations that, due to the steep slope in M31's disk, systematically increase in magnitude from one side of the galaxy to the other. The NW side of M32 tends to suffer from more severe contamination than the SE side, even in the M31 subtracted image. The impact of this variable contamination on the M32 isophote fits is tested by dividing the galaxy along its minor axis into halves — toward and away from the nucleus of M31 — and performing independent ellipse fits to both halves, as well as to the whole. Figure 8b shows the de Vaucouleurs law $\Delta\mu$ profiles that result from the ellipse fit to the SE half (triangles), the NW half (squares) and the entire body of M32 (circles). Out to a distance of $r \sim 250''$ the scatter in this plot is low, indicating that the μ profiles of the different fit regions are in good agreement. Beyond this radius, the M31 residuals on the NW side start to visibly affect the M32 surface brightness measurement. In Figure 9b and Figure 9d, similar results are found for the ϵ and ϕ' profiles, with one exception. The NW half B-band ellipse fit produces ϵ and ϕ' profiles that are noisier than the others, and fixed beyond $\sim$250$''$. The I-band fits of this same region, however, are in agreement with those of the SE half, indicating that the true profile is symmetric and that the departures seen in the B-band are most likely due to M31 disk residuals. Further evidence reinforcing the symmetry

of ϵ and ϕ' is seen in the final two panels of Figure 5. In these residual images, the best-fit ellipse model for M32 is modified to have constant ϕ' (Fig. 5c), and constant ϵ (Fig. 5d), with both held at their inner radius values. The systematic features visible in these images in comparison to the best-fit residual image (Fig. 5b) illustrates the significance and symmetry of the ϵ and ϕ' variations with radius. Based on these tests, the cleaner SE half of the galaxy is ultimately adopted for the best-fit μ, ϵ and ϕ' profiles.

The final concern relates to the accurate determination of the sky, since the outer isophotes of M32 have surface brightnesses that are a small fraction of the sky level ($\sim$1–2% at $r \sim 300''$). Regions well away from M32 that appear to be clean of contaminating spiral arms or dust lanes, are used to estimate the sky. To investigate potential systematic errors that this may introduce, the robustness of the μ profiles is tested in the final two panels of Figure 8. In Figure 8c, residuals computed with our best estimate for the sky background (triangles) are compared to those that would result from a misestimate of the sky (squares, circles). This extreme example shows that even a large $\pm$1% sky error cannot account for the low surface brightness depletion and excess features. This point is reinforced in Figure 8d, in which M32 residuals for the best-case sky subtraction (triangles) are plotted against curves that represent the expected residuals for a theoretical de Vaucouleurs law profile with various degrees of sky subtraction error. The predictable effect of sky errors does not match the M32 residuals, indicating that sky misestimates are not responsible for the low surface brightness features.

Together, Figure 8 and Figure 9 show the reliability of the μ, ϵ and ϕ' profiles out to at least $r \sim 250''$ and demonstrate that the profile features associated with the depletion zone and excess region cannot be reconciled with background subtraction errors. To further illustrate this point, a color comparison of the residuals is investigated.

4.4.2. Color Comparison of Extended Isophotes

It is impossible to remove every small-scale M31 disk feature; therefore, the possibility that the extended isophotes of M32 are dominated by a chance superposition of these residual features is investigated. Although background contamination would generally produce asymmetric features, a color comparison of the extended isophotes, to those of the sky and the M31 disk residuals provides a useful complementary test. Using the B- and I-band images, a color-index map is made of M32 and its surroundings. In Figure 10, different sections of this map are sampled in $10'' \times 10''$ boxes and plotted on a $B - I$ versus μ_I diagram. Finely sampling each isophote of M32, from the core ($r < 10''$) to the most extended isophotes ($r > 300''$), the mean value of the M32 color index is determined to be $B - I = 1.9$ with relatively small scatter for regions within $r < 150''$. An envelope enclosing the locus of points representative of M32 is plotted in Figure 10a. The points in this panel sample three distinct M31 residual regions (stars, crosses, squares) as well as smooth patches of uncontaminated sky (triangles).

In the three remaining panels (Figs. 10b–d) this background sample (small crosses) is plotted against points (circles) that represent three subregions within M32's measured isophotes: the main body ($r < 150''$); the depletion and excess regions ($150'' < r < 300''$); and the most extended measured isophotes ($r > 300''$). The consistency of the $B - I$ color index in regions out to $r \sim 300''$ compared to the colors of the field samples, supports the claim that the excess light is truly associated with M32 and not with M31 or sky variations. Even beyond $r > 300''$, the color spread around the M32 mean color is relatively small down to $\mu_I^{\mathrm{lim}} = 23.5$ mag arcsec^{-2}.

How does the broadband color of the tidal debris in M32's outskirts compare to that of the stellar stream found by Ibata et al. (2001) in the M31 halo? The $B - I$ color is about 2 for M32's outer tidal excess (Figs. 4 and 10). Since $V - I \approx 0.5(B - I)$ across a wide range of stellar types (Bergbusch & VandenBerg 2001), the $V - I$ color index for M32 is estimated to be about 1. At face value, the luminous giants near the tip of the red giant branch detected by Ibata et al. are redder than this with $V - I$ spanning the range 1–3 (see Fig. 2c of their paper). However, it should be noted that the *integrated* $V - I$ color of an old stellar population is comparable to the color of stars near the base of the red giant branch (cf. Guhathakurta et al. 1998), which corresponds to $V - I \sim 1$ for the stream. Thus, the expected $V - I$ color of the integrated stream agrees quite well with that of M32's outer tidal material.

5. NGC 205

The observational data for NGC 205 are similar to those presented for M32 above; the same surface photometry and analysis methods are used. The situation is somewhat easier for NGC 205 with regard to contamination by M31 disk light, so extensive tests of the robustness of the results are not carried out for this galaxy. The interpretation of the NGC 205 data, however, are far more complicated for a few reasons: (1) the satellite is significantly flattened, making it difficult to draw conclusions from our simulations of spherical, non-rotating satellites; (2) the inner μ profile is complicated, intermediate in Sersic index n between an exponential law ($n = 1$) and a de Vaucouleurs law ($n = 4$) but not a good fit to any n value, making it difficult to estimate the intrinsic profile of NGC 205; and (3) the intrinsic brightness distribution is patchy in places, with hints of dust lanes and star forming regions, complicating the search for subtle departures from isophotal symmetry due to tidal effects.

Surface photometry is performed using the task ELLIPSE on M31-subtracted images; however, unlike the M32 isophotes, the two bands are not fit independently. Due to incomplete coverage in the I band, only the B band is used for the determination of the best-fit elliptical isophotes. The ϵ and ϕ' ($|\phi'_{\mathrm{NGC\ 205}}| = |\phi_{\mathrm{NGC\ 205}} - 132.9°|$) profiles from this fit are then used to compute the I-band photometry. Though this is not expected to have a major impact on the resulting profiles, it does mean that the ellipticity ϵ and position angle ϕ' profiles are only fit in one band. Surface photometry is measured out to a limiting semi-major axis length of $r \sim 720''$ (2.7 kpc) with a limiting surface brightness of $\mu_B^{\mathrm{lim}} = 27.0$ mag arcsec^{-2}. In Figure 11, a B-band image of NGC 205

is shown at two different contrast levels, with elliptical isophotes ranging from $140'' < r < 660''$ overlaid to illustrate the low surface brightness region in which pronounced isophote twisting is observed. In Figure 12, the results of the best-fit elliptical isophotes are presented as radial profiles of μ, ϵ and ϕ' in log-linear and de Vaucouleurs coordinates.

Comparisons of the measured NGC 205 brightness profile to those of Hodge (1973) and Kent (1987) show general agreement. The data confirm that the profile is not well fit by any one analytic profile, but instead, is intermediate between an exponential and $r^{1/4}$ law as noted by Kent. Like M32, the profile fits are highly dependent on the radius range chosen. As is evident in the log-linear plot of Figure 12, the profile is well fit by an exponential law with a scale length $r_{B,R,I}^{\text{exp}} = 150''$, over the range $75'' < r < 250''$ and $r_{B,R,I}^{\text{exp}} = 170''$, over the range $150'' < r < 250''$. With respect to the $r_{B,R,I}^{\text{exp}} = 150''$ profile, a subtle downward break is detected at $r = 300''$ in both the B and I bands of the current data set, as well as in Kent's R-band data. The degree of the departure is inconsistent between the two sets. This may be due to increasing magnitude errors at isophotes that are approaching the Kent brightness limit. At radii beyond the limits of either Kent or Hodge ($r > 500''$), the surface brightness returns to the projected exponential profile. Although the magnitude of this break is subtle enough that neither Kent nor Hodge make note of it, its coincidence with shifts in ϵ and ϕ' provide compelling evidence for its significance.

The general shape of the measured ϵ curve, which rises with increasing radius to a maximum value of $e = 0.52$ at $r = 260''$ and then dips at larger radii, is in agreement with past results (Richter & Hogner 1963; Hodge 1973; Kent 1987). Beyond the peak at $r = 260''$ there is some discrepancy between the curves of Hodge and Kent. Kent shows a sharply dropping ellipticity out to the limit of his data at $r = 460''$, while Hodge sees only a slight dip at $r = 400''$ followed by a continued rise to the end of his data at $r = 480''$. The M31 removed CCD measurements confirm a slight dip beyond the maximum and then a gradual decline of the ellipticity out to and beyond $480''$. In the inner regions, the large amplitude ellipticity fluctuation at $r \sim 20''$, seen by both Richter & Hogner and Kent is also confirmed. Contrary to Hodge's speculation that this feature is an artifact of "a combination of poor statistics and systematic effects," our data indicate that it is significant.

The major-axis ϕ' profile shows a gradual increase out to a radius of $r = 260''$ and then a steady drop corresponding to a $30°$ twist out to the last measured isophote. This is in good agreement with Hodge, who measures continuous twisting out to the limit of his data.

6. Interpretation of Observations in Light of N-body Simulations

The previous sections focused on the detailed characterization of the M32 and NGC 205 observations. In the following section, these characteristics will be compared to numerical simulations, with the hope of determining whether they are tidally induced, and if so, using them to constrain the satellites' orbital parameters. A brief description of the simulations and their analysis is presented, along with results of their application to M32 and NGC 205. The details of the simulations

and the general trends of satellite interaction can be found in Johnston, Choi, & Guhathakurta (2002) (hereafter Paper I).

It is worth noting that the discussion in this section is based on the similarity in appearance between the observations and simulations, rather than a definitive proof that tides are responsible for the observed features. The models are not specifically tailored to match the intrinsic properties of M32 and NGC 205, or the precise potential of M31. Despite this, they provide a qualitative understanding of the physical mechanism that drives the tidal signatures. It has been shown that the two observed satellites have very different structural parameters. The current set of simulated spherically-symmetric satellites are well suited for the analysis of M32; however, they are not as applicable to NGC 205, due to its flattened structure. As a result, the bulk of the quantitative analysis is performed for M32, and a more conservative approach is taken for NGC 205. Fine tuning of the models and spectroscopic observations to determine satellite internal kinematics, both of which are in progress, will provide leverage to further refine orbital parameters and allow for a more comparable analysis of the two satellites in the future.

6.1.   The Simulations

In the numerical simulations, 64,000-particle, one-component, spherical satellites are followed for five radial oscillations as they orbit in a fixed three-component potential, representative of the disk, bulge, and halo of a parent galaxy. Particle interactions are computed using code developed by Hernquist & Ostriker (1992) and based on the basis-function-expansion technique. Of the five simulated satellites, four have Plummer initial density profiles and orbital eccentricity ranging from $0.10 < e < 0.88$ (Models 1–4). The fifth has a shallower Hernquist initial profile and an eccentricity of $e = 0.88$ (Model 5).

The analysis of the simulations is performed with a parallel and complementary approach to that of the observations. This facilitates direct comparison between the two. Snapshot "images" of each simulated satellite are generated by projecting the satellite particles onto a two-dimensional plane and smoothing the resulting distribution. The images for a range of orbital phases and viewing angles are then analyzed with the same ellipse-fitting technique that is used for the M32 and NGC 205 images. The resulting trends in the surface brightness μ, ellipticity ϵ and position angle ϕ' profiles with orbital eccentricity, phase and viewing angle, are used to guide the interpretation of the M31 satellite observations.

6.2.   Viewing Angle

The detection of isophote twists in the simulated satellites is a signature of an inclined orbital plane. By contrast, when viewed from within the orbital plane, the fitted ellipses line up along the direction of motion and twists are not observable. Comparing simulations viewed at angles of $0°$,

30°, 60°, and 90° from the orbital plane (edge-on to face-on), isophote twists are measurable for $i \gtrsim 30°$, indicating that even at low inclinations, the effects of tidal twisting are observable. Our study shows that for $i \gtrsim 30$, the observed quantities have a negligible dependence on the viewing angle. This simplifies the analysis, but it also limits the viewing angle determination to "edge-on" vs. "face-on".

The observed satellites, M32 and NGC 205, exhibit varying degrees of isophote twisting, indicating face-on viewing angles; however, in the case of NGC 205, where the assumption of intrinsic spherical symmetry may break down, a note of caution must be added. An intrinsically non-spherical satellite can exhibit isophote twists for $i = 0°$ if the satellite itself is inclined with respect to its orbital plane. NGC 205's flattened structure may have been tidally induced; but if not, little can be concluded about its orbital inclination.

6.3. Orbital Eccentricity and Phase

As defined in Paper I, the position angle ϕ' is the angle of the satellite semi-major axis, with respect to the satellite→parent galaxy vector. It is measured on the side of the satellite closer to the parent galaxy, so that $-90° < \phi' < 90°$. As will be shown in §6.4, the probable sense of M32's projected orbit is clockwise around M31 so this is hereby adopted for the sign convention of ϕ' for both galaxies.

For circular orbits of spherical satellites $\phi'(r_{\rm break})$, the position angle of the $r_{\rm break}$ isophote, and $d\phi'/dr(r_{\rm break})$, describing the isophote twist, both have the same orientation (Johnston et al. 1999a). The fact that neither M32 nor NGC 205 exhibits this trend between $\phi'(r_{\rm break})$ and $d\phi'/dr(r_{\rm break})$ reveals that these satellites are not likely to be on circular orbits. In addition to the relationship between $\phi'(r_{\rm break})$ and $d\phi'/dr(r_{\rm break})$, in the case of M32, three other profile features are suggestive of a highly eccentric orbit: (1) the triple break in the ϕ' profile, (2) the ratio $r_{\rm break}/r_{\rm tide}$ and (3) the ratio $r_{\rm break}/r_{\rm distort}$. The diagnostics $r_{\rm break}$ and $r_{\rm distort}$ are empirically measured radii that characterize the μ and ϵ profiles. Specifically, $r_{\rm break}$ is the radius at which a sharp change is measured in the slope of the μ profile, and $r_{\rm distort}$ is the corresponding radius for the ϵ profile (Paper I). By contrast, $r_{\rm tide}$ is an estimate for the theoretical King tidal radius.

In Figure 13, the best-fit elliptical isophote profiles for M32 are compared to those of a simulated satellite on a highly eccentric orbit ($e = 0.88$) that is approaching apocenter (Model 4). Striking similarities seen in the μ, $\Delta\mu$, ϵ, and ϕ' profiles of the observed and the simulated satellite imply that the M32 features have tidal interaction origins. The $\Delta\mu$ profile is based on the "inner" de Vaucouleurs law fit for M32, and the intrinsic μ profile for the simulated satellite. The $M32\mu$, $\Delta\mu$ and ϵ profiles have generic shapes that are common for many of the simulated snapshots, independent of the satellite's orbit or phase. The ϕ' profile, however, with its multiple twists — each of which is coincident with either a μ or ϵ feature — is more atypical. The triple twist in ϕ', which is seen only in simulated satellites approaching apocenter of highly eccentric orbits, provides

a clue not only about M32's orbital eccentricity, but also its orbital phase.

The second signature of an eccentric orbit is $r_{\rm break}/r_{\rm tidal}$, the ratio of the observed break in the μ profile and the classically defined theoretical King tidal radius. In the simplifying case of a circular orbit, $r_{\rm tide,\,peri}$ [defined in equation (1)] depends only on the mass of the satellite galaxy, the enclosed mass of the parent, and the distance between them. To investigate the likelihood that M32 is on such an orbit, its tidal radius is calculated based on the following: M32 is assumed to have a circular orbit; the projected distance between M32 and M31 is adopted as their separation; $M_{\rm M32} = 2.1 \times 10^9~M_\odot$ is adopted; and M31's enclosed mass is calculated by modeling it as an isothermal sphere, $M_{\rm M31} = v_{\rm circ}^2 R_{\rm proj}/G$ with $v_{\rm circ} = 240$ km s^{-1}. The resulting $r_{\rm tide}^{\rm M32} = 310''$ (1.2 kpc) is only weakly dependent on $M_{\rm M32}$ and $M_{\rm M31}$, so the main uncertainty is in the assumption that $R_{\rm proj}$ is the true separation. A measured $r_{\rm break}^{\rm M32} = 140''$ (0.54 kpc), results in $r_{\rm break}^{\rm M32}/r_{\rm tide}^{\rm M32} \sim 0.5$, which is a conservative upper limit since $R_{\rm proj}$ is a lower limit to the true separation. The top panels of Figure 14 show the orbital eccentricity and phase dependence of this ratio. The ratio $r_{\rm break}/r_{\rm tidal}$ typically has values of unity or greater for near-circular orbits. Only in highly eccentric orbits with $e \gtrsim 0.5$ does it drop as low as $r_{\rm break}/r_{\rm tide} \sim 0.5$, suggesting that M32 is on this latter type of orbit.

The final clue to M32's orbital eccentricity is the coincidence of $r_{\rm break}$ to $r_{\rm distort}$, the radius associated with the onset of isophotal elongation. For the intrinsically-spherical, simulated satellites, $r_{\rm distort}$ is defined as the radius at which $\epsilon > 0.02$; however, for the observations, due to the non-spherical nature of real galaxies, $r_{\rm distort}$ is modified to a more general definition of the radius at which the ellipticity departs sharply from the inner radius value. For M32 this is seen to occur at $r_{\rm distort}^{\rm M32} = 150''$ (0.57 kpc), resulting in $r_{\rm break}/r_{\rm distort} \sim 1.0$. In Figure 13, the locations of $r_{\rm break}$ and $r_{\rm distort}$ are shown as dotted vertical lines in the $\Delta\mu$ and ϵ plots, respectively. In the lower panels of Figure 14, the orbital eccentricity and phase dependencies of the ratio $r_{\rm break}/r_{\rm distort}$ indicate that $r_{\rm break}/r_{\rm distort} \geq 2.0$ for near-circular orbits and approaches unity only for the most eccentric orbits, again supporting the theory that M32 is on such an orbit. Unlike $r_{\rm tidal}$, both $r_{\rm distort}$ and $r_{\rm break}$ are directly observable, making this deduction less model dependent and more robust than the previous one about $r_{\rm break}/r_{\rm tide}$.

In addition to constraining M32's orbital eccentricity, the three arguments above indicate that M32 is currently in an orbital phase away from pericenter. In particular, the fact that the lower limit for $r_{\rm tide}$ is a factor of two greater than both $r_{\rm break}$ and $r_{\rm distort}$ provides robust evidence that M32 cannot be at pericenter. Severe tidally induced distortions are not expected to be seen interior to the tidal radius of a satellite at pericenter, $r_{\rm tide,\,peri}$. Following this line of reasoning, $r_{\rm tidal,peri}$ can be estimated using $r_{\rm break}$ and $r_{\rm distort}$ alone. As is shown in Figure 15 of Paper I, $r_{\rm tidal,peri} \approx 0.5 r_{\rm break}$ for $r_{\rm break} \sim r_{\rm distort}$. This corresponds to $r_{\rm tide,\,peri} \approx 0.3$ kpc; and translates to a M32–M31 pericenter separation of $R_{\rm peri} \sim 0.7$ kpc, via the King formula. Even the most conservative estimate of $r_{\rm tide,\,peri} \approx r_{\rm break}$ implies an upper limit $R_{\rm peri} \lesssim 1.7$ kpc that is much less than $R_{\rm proj} = 5.5$ kpc. Adopting $R_{\rm peri} = 0.7$ kpc, and an orbital eccentricity $e = 0.88$ (based on Model 4 of the simulations), M32's apocenter is estimated to be $R_{\rm apo} \approx 10.5$ kpc. If M32 is currently near apocenter, as the ϕ' triple twist suggests, M32 must be at least $8 - 9$ kpc in the

foreground or background of M31's core. This is well within the current ± 100 kpc uncertainty in the relative distances to M32 and M31.

6.4. Direction of Motion

For circular orbits, $\phi'(r_{\text{break}})$ and $d\phi'/dr(r_{\text{break}})$ are related to the direction of the orbit and can therefore be used to constrain the satellite's projected motion. Unfortunately, these relationships have a phase dependence for eccentric orbits. As a result, the projected motions of M32 and NCG 205 are indeterminable from their isophote orientations alone. In the case of M32, the orbital direction can be recovered since its phase has been independently determined.

If M32 is indeed on a highly eccentric orbit approaching apocenter, as suggested in §6.3, then the simulations indicate that $\phi'_{\text{M32}}(r_{\text{break}})$ should be negative (Fig. 11 of Paper I). The orientation of ϕ' is defined with respect to the direction of motion, implying that M32's r_{break} isophote, on the inner side of its orbit, should be pointed away from its direction of motion.

One caveat of the above argument is that the non-spherical nature of real galaxies implies that there is a non-zero intrinsic value for the position angle, ϕ'_{inner}. Instead of simply looking at the sign of $\phi'(r_{\text{break}})$, one must instead consider the sign of the *change* in position angle relative to the interior intrinsic value, $\Delta\phi'(r_{\text{break}}) \equiv \phi'(r_{\text{break}}) - \phi'_{\text{inner}}$, where $\phi'_{\text{inner}} = -20.0°$ for M32's inner isophotes. For M32, $\Delta\phi'(r_{\text{break}})$ has an absolute value of 5.2°. As discussed above, prior knowledge of this satellite's orbital phase and eccentricity indicates that $\Delta\phi'(r_{\text{break}})$ must be negative, and this implies that M32's projected orbit is clockwise about M31 as indicated in Figure 15.

6.5. Comparison of M32 and NGC 205 Intrinsic Profiles

The generic characteristics shared by all of the simulated satellites are a depletion zone at small radii and an excess region at large radii (Fig. 6 of Paper I). This is an expected consequence of tidal stripping and flux conservation that is independent of orbital parameters or the satellite's initial profile. Both regions have μ profile breaks associated with their onset: a gradual *downward* (negative) break in the case of the depletion zone, and an abrupt *upward* (positive) break in the case of the outer excess region.

Though not easily discernible from the μ profiles, both breaks are generally evident in the $\Delta\mu$ residual plots. To mimic the analysis of real galaxies, for which intrinsic profiles are unknown, r_{break} is measured using only the μ profile. The detection criteria for r_{break} is not biased towards either positive or negative departures; however, it does depend on the sharpness and magnitude of the profile slope change. As a result, r_{break} tends to be preferentially associated with the sharp, outer break. Only in the simulated satellite of Model 5, which has a shallow initial density profile, is the inner "depletion zone" break detected as r_{break}. The satellites in Models 4 & 5 have identical

orbital parameters and differ only in their initial density profile, revealing a connection between the intrinsic profile and its measured parameters after interaction.

In the observed μ profiles, r_{break} is positive for M32 and negative for NGC 205. The difference in the intrinsic profiles of the two satellites — NGC 205's is much shallower than M32's — hints at a profile dependent detection bias, as suggested by the simulations. For M32, it is evident from the $\Delta\mu$ profiles (Fig. 13) that r_{break} corresponds to an outer "excess region" break. For both M32 and the Model 4 satellite, though not initially identified due to its gradual nature, the inner "depletion zone" break is clearly visible. By contrast, because of NGC 205's shallow intrinsic profile, the stripping of material results in an inner "depletion zone" break that is sharp enough to be measured (Fig. 12). Unfortunately, there is no evidence for the accompanying outer "excess region" break that would reinforce its identification. This may simply be beyond the current sensitivity limit of the observations.

6.6. Constraints on Mass Loss

It is shown in Paper I that constraints can be placed on satellite mass-loss rates from surface photometry alone. Measurements of the extra-tidal population of M32 and NGC 205 are used to make order-of-magnitude estimate for their instantaneous, fractional mass-loss rate per orbital period,

$$\frac{df}{dt} = \frac{\pi^2 r_{\text{break}}^2 \Sigma_{\text{break}}}{m_{\text{break}}}, \tag{2}$$

as discussed in Paper I. The ratio of $\Sigma_{\text{break}}/m_{\text{break}}$, the surface density at r_{break} to the mass enclosed within this point, can be calculated from the μ profile, assuming a constant mass-to-light ratio. The derived rates for M32 and NGC 205, $df/dt|_{\text{M32}} = 0.38$ and $df/dt|_{\text{NGC 205}} = 2.95$, are shown in the last column of Table 2.

The high apparent destruction rates for both satellites should be qualified by two factors. The first is that although the simulations show that surface brightness derived rates are accurate to within order unity for near-circular orbits, this relationship degenerates with eccentricity. For eccentric orbits, df/dt is phase dependent, as illustrated in Figure 16 of Paper I. Mass loss estimates are reliable near pericenter, where the bulk of mass loss occurs; however, away from this phase, they are systematically high by up to half an order of magnitude. The reason for this overestimate is that away from pericenter, only a fraction of the extra-break material that is generally heated, yet bound, will be lost on the current orbit. The second factor is that df/dt is an instantaneous, phase-dependent rate that provides a direct measure of the total mass loss per orbit only when df/dt is constant, as in the circular case. For eccentric orbits, it must be integrated over the entire orbit to calculate the total orbital mass loss. Given these caveats, the presented df/dt should be considered only as upper limits for the instantaneous fractional mass-loss rate. As such, they should

not be used to extrapolate a destruction rate.

6.7. Future Directions

The simulations presented in this paper and Paper I provide useful pointers about the nature of tidal interaction in M32 and NGC 205, despite the fact that they are not tuned to mimic these satellites. Future simulations will explore combinations of satellite orbital eccentricities and phases that are constrained by the actual distances and radial velocities measured for M32, NGC 205 and M31. Furthermore, the simulated satellites almost certainly depart from real galaxies in the assumption that mass follows light. In the future, two-component (stars and dark matter) model satellites will be incorporated into the simulations.

7. Implications for M32's Surface Brightness and Luminosity Evolution

In a plot of L versus μ, cEs lie on the extension of the giant E galaxy track, typically $\sim 2 - -3$ magnitudes fainter in luminosity and $\sim 1 - -2$ magnitudes brighter in surface brightness (Ziegler & Bender 1998). At the faint, low surface brightness extreme is M32. Due to its proximity to M31, most formation theories suggest that M32 is the remnant of a galaxy that has been stripped through tidal interaction. Numerous galaxy types have been proposed as possible precursors; however, given its location in μ-L space, the most intuitive of these is a normal E galaxy. This theory can be investigated directly using our surface brightness observations.

The simulations presented in §6 indicate that, despite the loss of a substantial amount of mass in their outer regions, the interior portions of the dwarf satellites' μ profiles remain largely unaffected [(Fig. 13 (upper two panels on the right)]. While the simulations are admittedly simplistic, in the case of M32, this assumption is probably a reasonable one. One particular concern is that the present simulations involve single-component satellites in which mass follows light. By contrast, real satellites are expected to have extended dark halos. Fortunately, such a halo would tend to further buffer the interior of the satellites from tidal stripping, thereby reinforcing this finding.

Guided by the notion that the interior brightness profile of M32 is pristine and the *assumption* that the original profile (prior to tidal stripping) obeyed a de Vaucouleurs law, one can quantitatively address the question of whether the unusual location of this galaxy in a μ-L plot could be the result of tidal stripping of a normal E galaxy. Of the three $r^{1/4}$ law fits presented in Figure 6 of §4.3, the one labeled "extreme-inner" (fit to inner $r = 10''$–$30''$) is most likely to represent the intrinsic profile of M32. The resulting estimates of M32's intrinsic effective surface brightness are $\mu_I^{\mathrm{eff}} = 18.41$ mag arcsec^{-2} and $\mu_B^{\mathrm{eff}} = 20.15$ mag arcsec^{-2}. Adopting the "standard" ($r_{\mathrm{eff}} = 29''$) fit as representative of M32's current de Vaucouleurs law profile leads to current M32 values of $\mu_I^{\mathrm{eff}} = 17.53$ and $\mu_B^{\mathrm{eff}} = 19.43$, in good agreement with historical results. These values imply an evolution of $\Delta\mu_I^{\mathrm{eff}} = 0.88$ and $\Delta\mu_B^{\mathrm{eff}} = 0.72$.

The luminosity evolution is estimated by comparing its current luminosity to that of the intrinsic $r^{1/4}$ law profile fit assumed for M32. The three de Vaucouleurs law fits are integrated to estimate the intrinsic luminosity of M32 as a function of enclosed radius. These "curves of growth" are shown in Figure 16 (long-dashed, short-dashed, and dotted lines for the "standard", "inner", and extreme-inner" fits, respectively), along with the curve of growth based on the *actual* brightness profile of M32 (solid line).

These curves overlap with one another interior to the inner break $r = 50''$ and diverge beyond this radius, consistent with the expectation that the majority of the luminosity evolution occurs in the depletion zone. The "standard fit", which most closely follows M32's observed integrated luminosity curve through the depletion zone, underestimates the total magnitude at large radii, due to the tidal excess feature discussed in §4.2. The curves of the two inner-radius fits on the other hand are less biased by the depletion zone and therefore provide a more conservative estimate for M32's intrinsic luminosity. Adopting the "extreme-inner" fit as M32's intrinsic profile results in a modest luminosity evolution of $\Delta B_{\mathrm{M32}} \sim 0.1$ and $\Delta I_{\mathrm{M32}} \sim 0.15$, based on aperture photometry out to $r = 300''$. The adoption of total versus isophotal magnitudes would only impact the luminosity evolution by an additional $\sim 10\%$.

A comparison of M32's presently observed properties to estimates of its intrinsic properties, indicates a relatively small amount of evolution due to tidal effects. Although it is in the right direction — away from the family of E galaxies in the μ-L projection — the magnitude of this shift falls far short of explaining M32's position in terms of a tidally stripped/truncated normal E galaxy. Put another way, intermediate E galaxies have typical effective radii of $1.2 < r_{\mathrm{eff}} < 8.0$ kpc (Bender, Burstein & Faber 1993), whereas estimates of M32's intrinsic effective radius are in the range $37''$–$47''$ (0.14–0.18 kpc). This implies that M32 was intrinsically 'compact' even before any tidal stripping by M31, supporting Burkert's (1994a) theory that cEs are *formed* in a compact state — as opposed to being evolved into one. The bulges of spiral or S0 galaxies, typically intermediate in compactness between Es and cEs, cannot be ruled out based on the current analysis.

It is interesting to note that the integrated absolute magnitude of the Ibata et al. (2001) stream, estimated at $M_V(\mathrm{stream}) \approx -14$, is approximately 10% that of M32: $M_V(\mathrm{M32}) \lesssim -16$. The M32 value is derived from its curve of growth in the B band which yields $M_B(\mathrm{M32}) \lesssim -15$ (Fig. 16), and an interpolated $B - V$ color of about unity (see §4.4.2). Moreover, the estimated amount of luminosity evolution in M32 due to tidal stripping is about 0.1 mag (see above). Thus accumulated tidal debris from M32 can adequately account for the overall brightness of the stream.

8. Summary

This paper presents surface photometry of M31's two nearest satellites, M32 and NGC 205, and a comparison to N-body simulations. Details of the simulations are in the companion paper Johnston, Choi & Guhathakurta (Paper I). The primary objectives of this work are to investigate

the impact of tidal interactions on the morphology and evolution of dwarf satellite galaxies and to place constraints on the satellite orbital parameters. The main points are outlined below:

- Large-format B- and I-band CCD mosaic images of the M31 sub-group form the basis of this study. Global ellipse fits are used to model and subtract M31's contaminating disk light, enabling measurement of the faint outer isophotes of M32 and NGC 205 where tidal signatures are most prominent.

- The surface brightness profile of M32 has traditionally been fit by a de Vaucouleurs $r^{1/4}$ law, but there is a clear excess of light in the outer parts ($r \gtrsim 140''$) relative to the "standard" fit. The excess is coincident with elongation and twisting of the isophotes. There is also a downward break in the μ profile at $r \sim 50''$ in the inner region of M32; this too is accompanied by isophote twists. The intrinsic μ profile of NGC 205 is more complex than M32's, intermediate between a simple exponential and $r^{1/4}$ laws, and is in good agreement with previous measurements.

- The robustness of the M32 results is demonstrated through a series of tests. The measured isophotal parameters—surface brightness, ellipticity, and orientation—are robust out to at least $r \sim 250''$ and share the following characteristics: (1) insensitive to details of M31 disk modeling and sky subtraction errors; (2) symmetric about M32 despite the stark difference in the quality of the inner versus outer M31 disk list subtraction; and (3) $B - I$ color index that is consistent with the inner parts of M32.

- The M32 and NGC 205 measurements are compared to numerical simulations of single-component, spherical, non-rotating, satellites, orbiting in a fixed, three-component parent galaxy potential. The simulations provide insight into the nature of tidal interaction even though they are not tailored precisely to M32 and NGC 205.

- The surface brightness profiles of tidally disrupted simulated satellites contain certain generic features reminiscent of those seen in the M31 satellites. These features include an excess region at large radii, a depletion zone at intermediate radii, and a central region that is largely unaffected by tidal interaction. Isophote elongation and twists are also common, though the details of the ϵ and ϕ' radial profiles are strongly dependent on orbital phase.

- A comparison between the observations and numerical simulations indicates that M32 and NGC 205 are likely both on highly eccentric orbits, away from pericenter, and that they are being viewed from outside their orbital plane. The sense of M32's projected orbit around M31 appears to be clockwise. M32 has a simpler (intrinsic) brightness distribution in its inner parts than NGC 205 and is a better match to our current suite of simulations; its orbital parameters are therefore better constrained.

- Empirical estimates are made of the effect of tidal stripping on M32's luminosity and effective surface brightness, based on an extrapolation of its inner surface brightness profile. The

estimated amount of change in L and μ_{eff} is far too small to be consistent with the theory that M32 evolved from a normal elliptical, and suggests instead that M32's precursor was intrinsically more compact than a typical E galaxy. This supports Burkert's (1994a) formation scenario for compact ellipticals such as M32 through a starburst and subsequent violent collapse within the potential well of a massive galaxy, though spiral or S0 bulges cannot be ruled out as possible precursors.

- While the current numerical simulations provide qualitative insight into the nature of tidal interaction in the M31 sub-group, future simulations will be tailored specifically to match the observed radial velocities, line-of-sight distances, and dynamical masses of M31, M32, and NGC 205. Other planned improvements include two-component satellites (stars and dark matter). Keck spectroscopy of individual red giant stars in the tidal region of M32 is being used to measure velocity and velocity dispersion profiles, which should better constrain the details of its interaction with M31.

9. Acknowledgements

REFERENCES

Aguilar, L. A., & White, S. D. M. 1986, ApJ, 307, 97

Arp, H. C. 1966, Atlas of Peculiar Galaxies (Pasadena: California Institute of Technology)

Bekki, K., Couch, W. J., Drinkwater, M. J., & Gregg, M. D. 2001, ApJ, 557, L39

Bender, R., & Nieto, J.-L. 1990, A&A, 239, 97

Bender, R., Burstein, D., & Faber, S. M. 1993, ApJ, 411, 153

Bergbusch, P. A., & VandenBerg, D. A. 2001, ApJ, 556, 322

Bica, E., Alloin, D., & Schmidt , A. A. 1990, A&A, 228, 23

Burkert, A. 1994a, MNRAS, 266, 877

Burkert, A. 1994b, Reviews of Modern Astronomy, 7, 191

Burstein, D., Faber, S. M., Gaskell, C. M., & Krumm, N. 1984, ApJ, 287, 586

Byrd, G. G. 1979, ApJ, 231, 32

Cepa, J., & Beckman, J. E. 1988, 200, 21

Cole, A. A., Gallagher, J. S., Mould, J. R., Clarke, J. T., Trauger, J. T., Watson, A. M., Ballester, G. E., Burrows, C. J., Casertano, S., Crisp, D., Griffiths, R. E., Grillmair, C. J., Hester, J. J., Hoessel, J. G., Holtzman, J. A., Scowen, P. A., Stapelfeldt, K. R., & Westphal, J. R. 1998, ApJ, 505, 230

Combes, F., Leon, S., & Meylan, G. 1999, A&A, 352, 149

Davidge, T. J., Rigaut, F., Chun, M., Brandner, W., Potter, D., Northcott, M., & Graves, J. E. 2000, ApJ, 545, L89

de Vaucouleurs, G. 1953, MNRAS, 113, 134

del Burgo, C., Peletier, R. F., Vazdekis, A., Arribas, S., & Mediavilla, E. 2001, MNRAS, 321, 227

Drinkwater, M. J., & Gregg, M. D. 1998, MNRAS, 296, L15

Evans, N. W., Wilkinson, M. I., Guhathakurta, P., Grebel, E. K., & Vogt, S. S. 2000, ApJ, 540, L9

Faber, S. M. 1973, ApJ, 179, 423

Grillmair, C. J., Freeman, K. C., Irwin, M., & Quinn, P. J. 1995, AJ, 109, 2553

Guhathakurta, P., Choi, P. I., & Raychaudhury, S. 2002, AJ, in prep

Guhathakurta, P., Webster, Z. T., Yanny, B., Schneider, D. P., & Bahcall, J. N. 1998, AJ, 116, 1757

Hernquist, L., & Ostriker, J. P. 1992, ApJ, 386, 375

Hodge, P. W. 1973, ApJ, 182, 671

Ibata, R., Irwin, M., Lewis, G., Ferguson, A. M. N., & Tanvir, N. 2001, Nature, 412, 49

Innanen, K. A., Harris, W. E., & Webbink, R. F. 1983, AJ, 88, 338

Irwin, M. J., & Hatzidimitriou, D. 1995, MNRAS, 277, 1354

Johnston, K. V., Choi, P. I., & Guhathakurta, P. 2002, AJ, submitted (Paper I)

Johnston, K. V., Sigurdsson S., & Hernquist, L. 1999a, MNRAS, 302, 771

Johnston, K. V., Zhao, H., Spergel, D. N., & Hernquist, L. 1999b, ApJ, 512, L109

Kent, S. M. 1987, AJ, 94, 306

King, I. R. 1962, AJ, 67, 471

King, I. R., & Kiser, J. 1973, ApJ, 181, 27

Kormendy, J. 1985, ApJ, 295, 73

Kormendy, J., & Djorgovski, S. 1989, ARA&A, 27, 235

Kuhn, J. R., Smith, H. A., & Hawley, S. L. 1996, ApJ, 469, L93

Leon, S., Meylan, G., & Combes, F. 2000, A&A, 359, 907

Majewski, S., Ostheimer, J. C., Patterson, R. J., Kunkel, W. E., Johnston, K. V., & Geisler, D. 2000, AJ, 119, 760

Mayer, L., Governato, F., Colpi, M., Moore, B., Quinn, T., Wadsley, J., Stadel, J., & Lake, G. 2001, ApJ, 547, L123

Mayer, L., Governato, F., Colpi, M., Moore, B., Quinn, T., Wadsley, J., Stadel, J., & Lake, G. 2001, ApJ, 559, 754

Moore, B. 1996, ApJ, 461, L13

Moore, B., Katz, N., Lake, G., Dressler, A., & Oemler, A. 1996, Nature, 379, 613

Moore, B., Lake, G., & Katz, N. 1998, ApJ, 495, 139

Moore, B., Lake, G., Quinn, T., & Stadel, J. 1999, MNRAS, 304, 465

Nieto, J.-L., & Prugniel, Ph. 1987, A&A, 186, 30

Nieto, J.-L. 1990, in Dynamics and Interactions of Galaxies, ed. R. Wielen (Berlin: Springer), 258

O'Connell, R. W. 1980, ApJ, 236, 430

Oh, K. S., Lin, D. N. C., & Aarseth, S. J. 1995, ApJ, 442, 142

Ostheimer, J. C., Majewski, S. R., Link, R., & Patterson, R. J. 2002, in preparation

Peletier, R. F. 1993, A&A, 271, 51

Peterson, C. J. 1974, ApJ, 190, L17

Richter, N., & Hogner, W. 1963, Astron. Nachr., 287, 267

Rose, J. A. 1985, AJ, 90, 1927

Sato, N. R., & Sawa, T. 1986, PASJ, 38, 63

Tonry, J. L. 1984, ApJ, 283, L27

Tonry, J. L. 1987, ApJ, 322, 632

Vazdekis, A., & Arimoto, N. 1999, ApJ, 525, 144

von Hoerner, S. 1957, ApJ, 125, 451

Wirth, A., & Gallagher, J. S. 1984, ApJ, 282, 85

Ziegler, B. L., & Bender, R. 1998, A&A, 330, 819
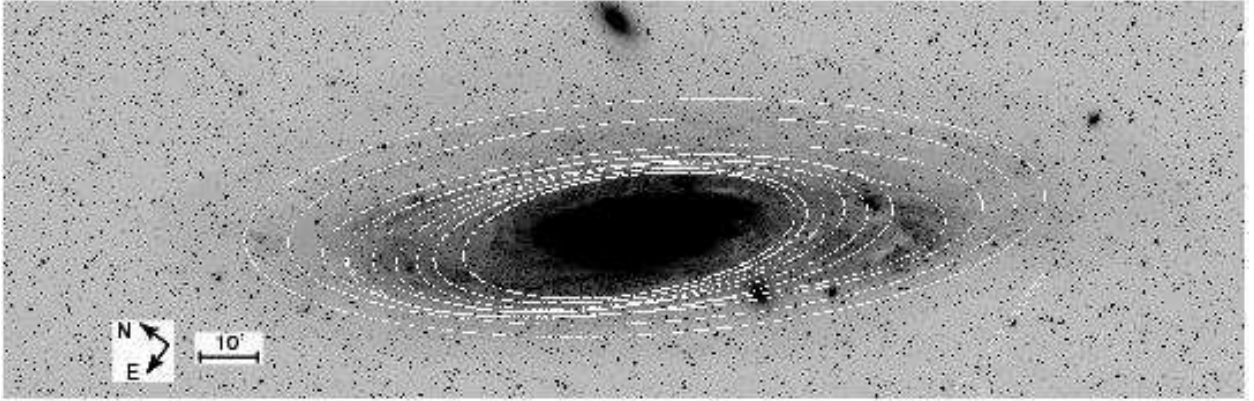
Fig. 1.— Grayscale representation of a B-band $1.3° \times 3.4°$ image of the M31 sub-group, covering M31, M32 and NGC 205. The best-fit elliptical isophotes of M31 over the semi-major axis range $30' < r < 70'$ are overlaid to illustrate the overlap with M32.
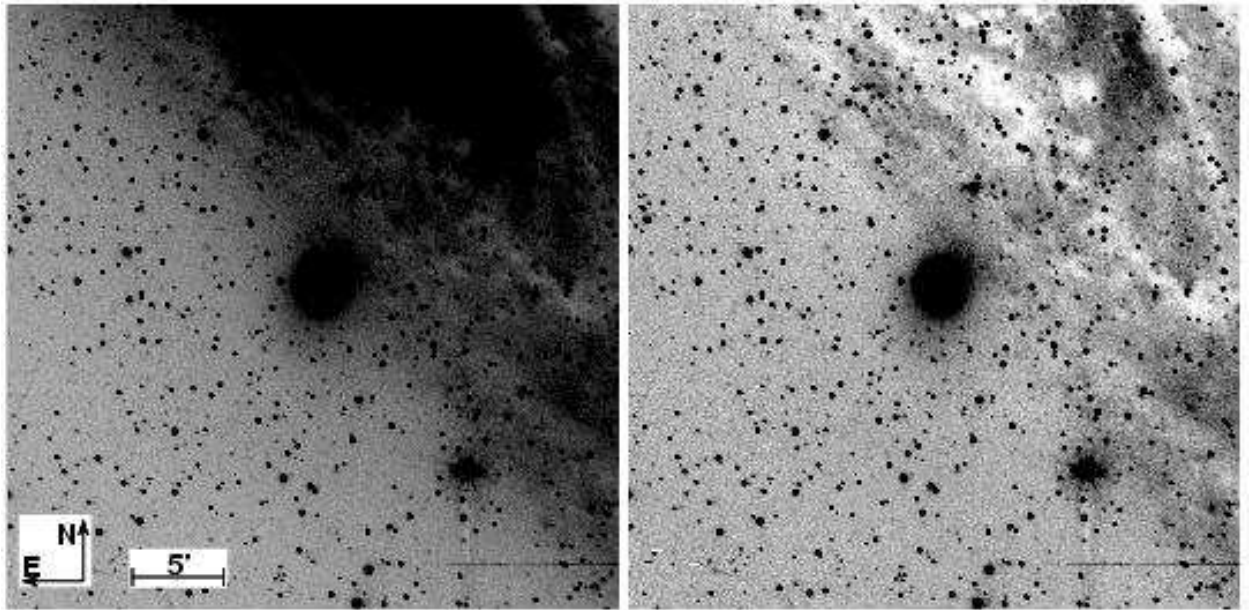
Fig. 2.— Grayscale representations of B-band images centered on M32 covering $34' \times 34'$ with (*left*) and without (*right*) M31's disk light contribution. Note the steep gradient in the background across M32 caused by the inclined disk of M31 (*left*) and the residual fine-scale structure (dust lanes, spiral arms, etc.) even after subtraction (*right*).
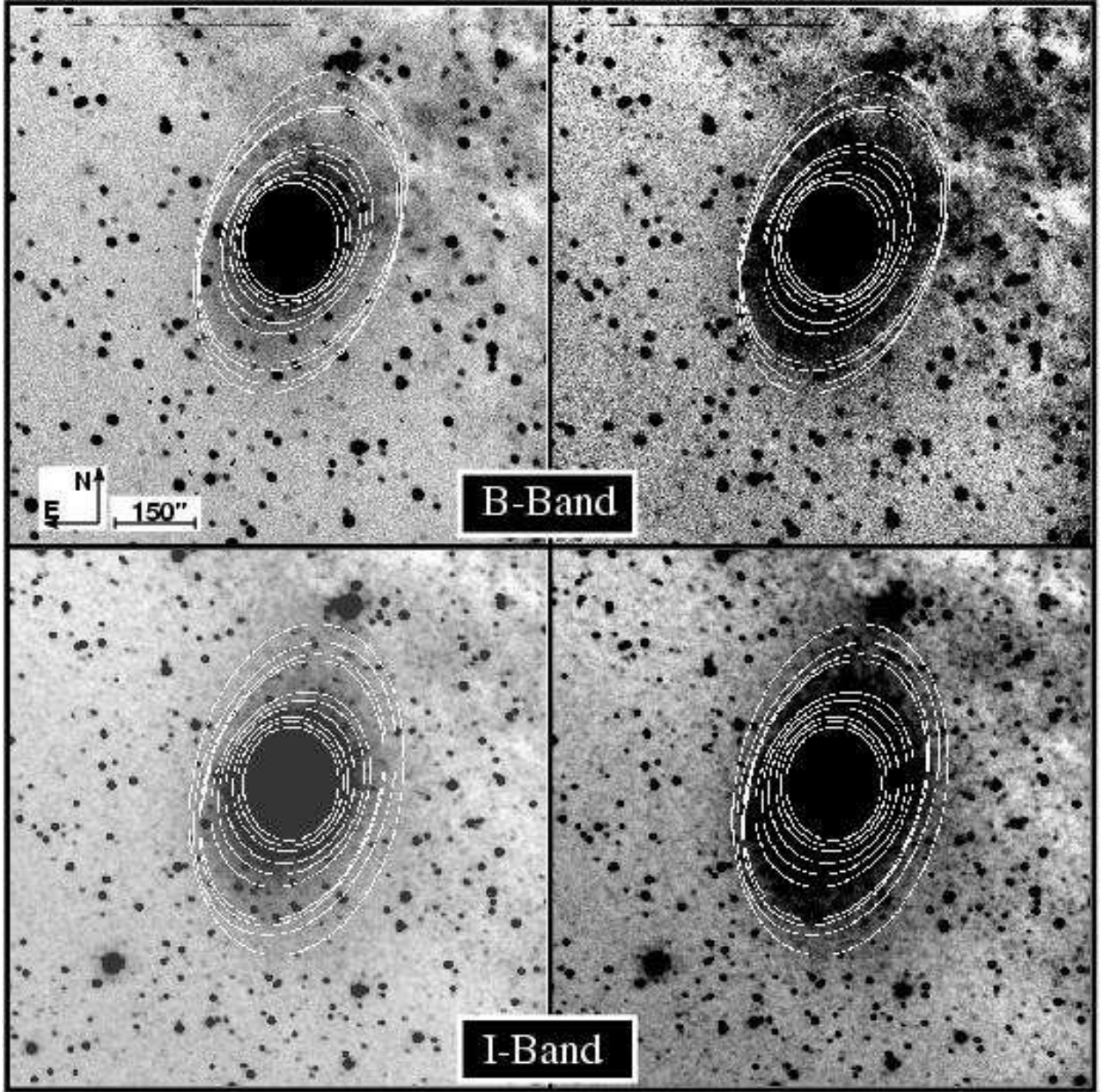
Fig. 3.— Grayscale representations of B- (*upper*) and I-band (*lower*) images of M32 covering $17' \times 17'$ at low (*left*) and high (*right*) contrast, with M31's disk light subtracted. Despite careful attempts to model the M31 light distribution, the NW portion of M32's outer isophotes is contaminated by residual M31 disk features. Best-fit elliptical isophotes of M32 in the semi-major axis range $100'' < r < 300''$ highlight the low surface brightness region in which signatures of tidal interaction are observed.
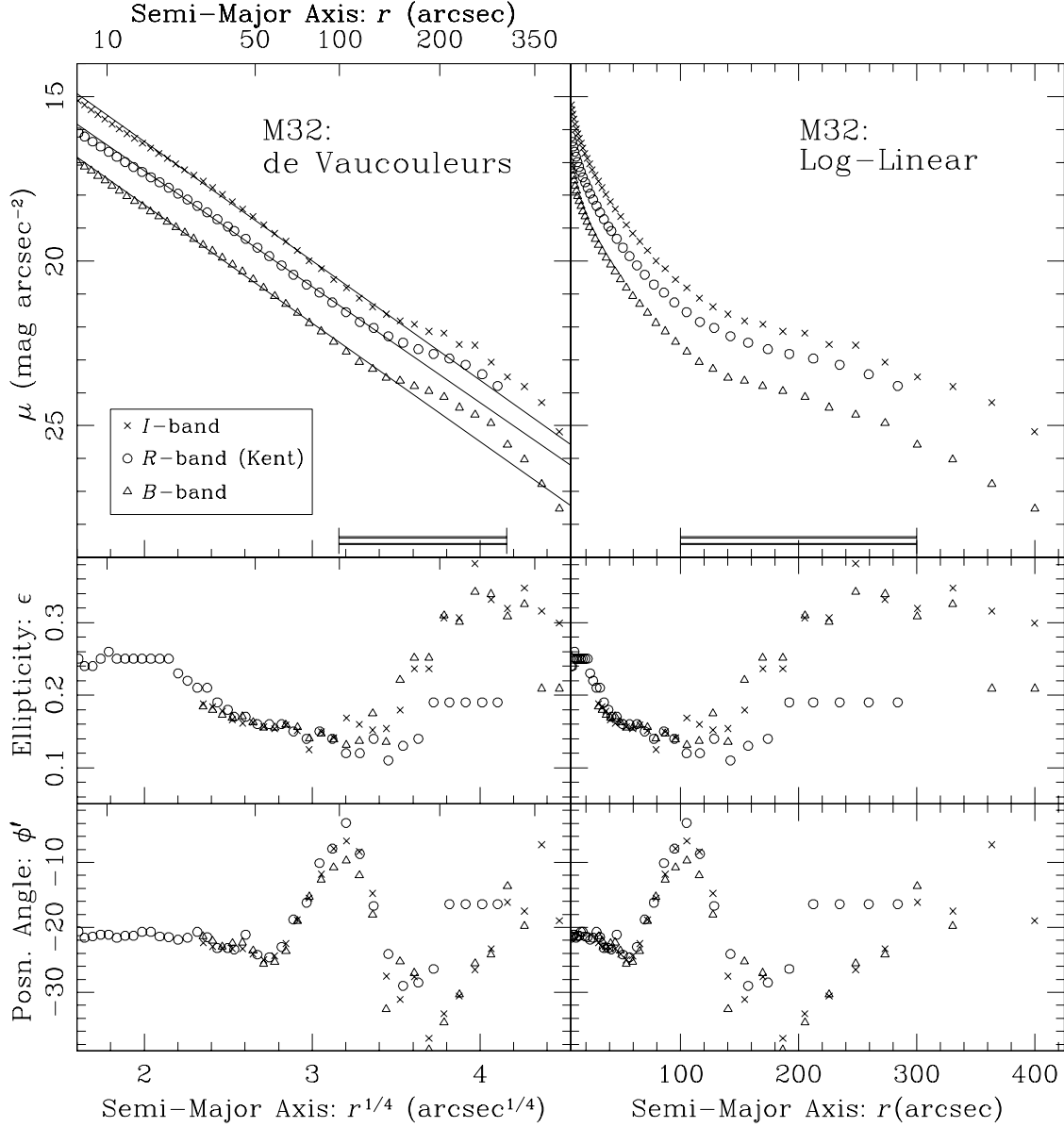
Fig. 4.— *Top to bottom*: Surface brightness μ, ellipticity ϵ, and position angle ϕ' (measured relative to the M32→M31 vector, positive in the direction N→E $[|\phi'_{M32}| = |\phi_{M32} - 1.1°|]$) of M32's isophotes versus semi-major axis length in de Vaucouleurs (*left*) and log-linear (*right*) coordinates in B (*triangles*), R (*circles*; Kent 1987), and I (*crosses*). The solid lines in the μ profile show $r^{1/4}$ law fits over a 5.5 mag range in $\mu_{I,R,B}$ over the semi-major axis range $10'' < r < 140''$ with $r^{\text{eff}}_{B,R,I} \sim 30''$ and $\mu^{\text{eff}}_{B,R,I} = 19.4, 18.6$, and 17.5 mag arcsec^{-2} ("standard" fit in Fig 6). Note that the outer excess light feature seen in the de Vaucouleurs projection at $r > 150''$ is coincident with sharp shifts in the ϵ and ϕ' profiles. The double bars marking the range $100'' < r < 300''$ in the μ plot show the region covered by the contours in Figure 3.
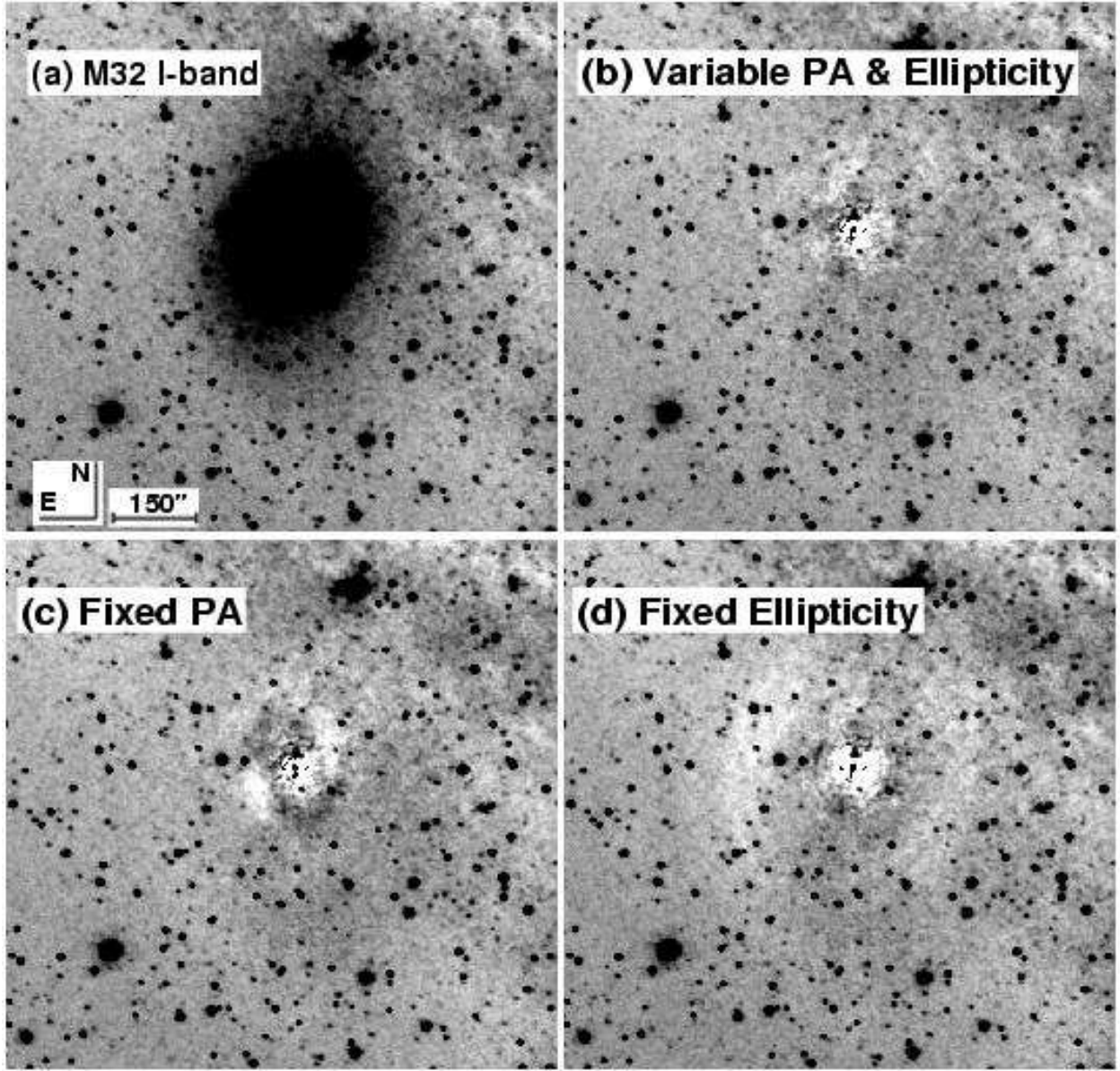
Fig. 5.— (*a*) Image of M32 in the *I*-band with M31's disk light subtracted.   (*b*) Residual image — original M32 image minus best ellipse fit in which the position angle ϕ' and ellipticity ϵ are allowed to vary with radius. The contrast level is the same as in (*a*).   (*c*) Same as (*b*), but with ϕ' held constant at the inner value of $\phi'_{\mathrm{inner}} = -20°$.   (*d*) Same as (*b*), but with ϵ held constant at the inner value of $\epsilon_{\mathrm{inner}} = 0.15$. The orientation and scale are as in Figure 3. Systematic features are visible in the lower panels; these illustrate the significance of the variations of ϕ' and ϵ with radius shown in Figure 4.
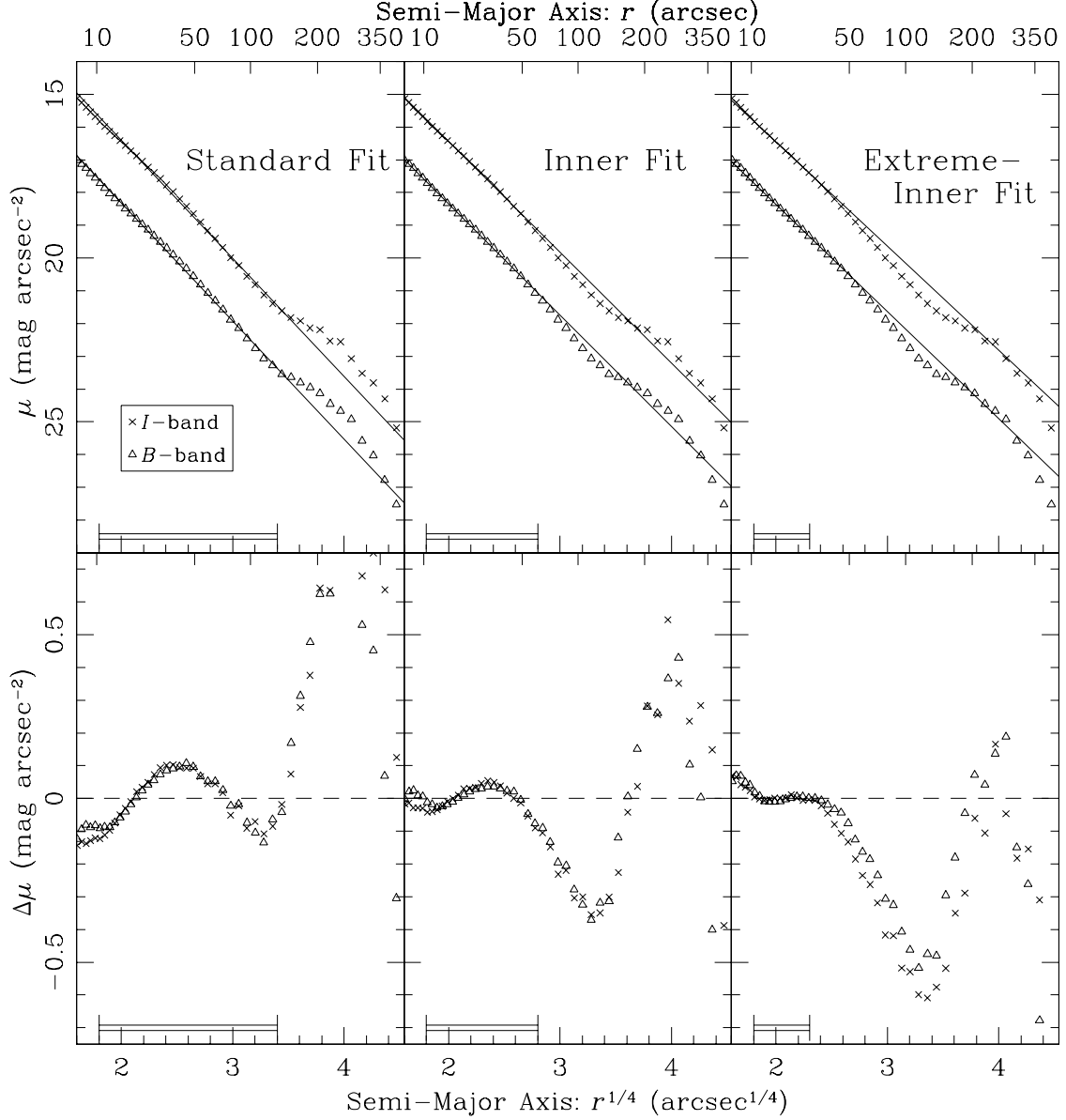
Fig. 6.— Surface brightness μ profiles (*top*) and residuals with respect to $r^{1/4}$ law fits $\Delta\mu$ (*bottom*) for M32 in B (*triangles*) and I bands (*crosses*). Standard (*left*), inner (*middle*), and extreme-inner (*right*) de Vaucouleurs law fits are shown (see §4.3 and Table 1). The range of radii fit is indicated by double bars along the bottom of each panel. Though the same μ profile is plotted in each of the three upper panels, the differences in the fits lead to significantly different interpretations of the residual profiles. Clear trends are seen from standard→inner→extreme-inner fit residual profiles: the prominence of the outer excess decreases; the strength of the depletion zone increases; and the systematic departure from the zero line decreases over the radial range of the fit.
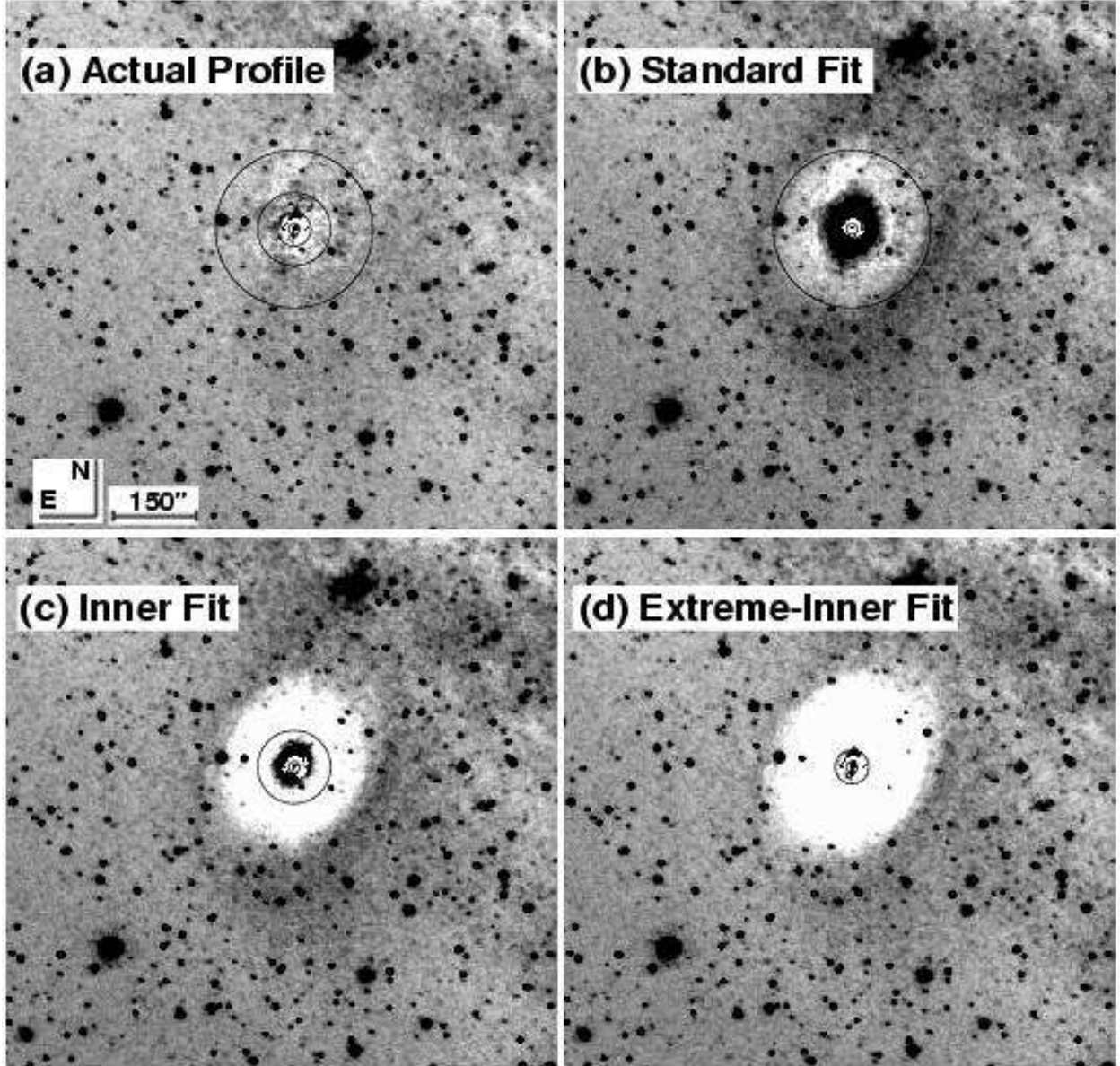
Fig. 7.— A comparison of various M32 *I*-band residual images: (*a*) Original minus best-fit ellipse model which follows M32's *actual* surface brightness μ profile [same as Fig. 5(*b*)];   (*b*) Original minus ellipse model based on the "standard" $r^{1/4}$ law fit to the μ profile (shown in Fig. 6);   (*c*) Same as (*b*), but for the "inner" $r^{1/4}$ law fit; and   (*d*) Same as (*b*), but for the "extreme-inner" $r^{1/4}$ law fit. The orientation and scale are as in Figure 5. The pair of concentric circles in each of panels (*b*–*d*) mark the inner and outer limits of the radial range over which the $r^{1/4}$ law is fit; all of these radii are also plotted in (*a*). The difference between M32 and the "standard" $r^{1/4}$ law fit not only varies systematically with radius over the range of the fit (Fig. 6) but is also seen to be symmetric in azimuth (*b*). Note, the azimuthally-symmetric depletion zone becomes more prominent and the outer excess becomes less prominent from (*b*→*c*→*d*).
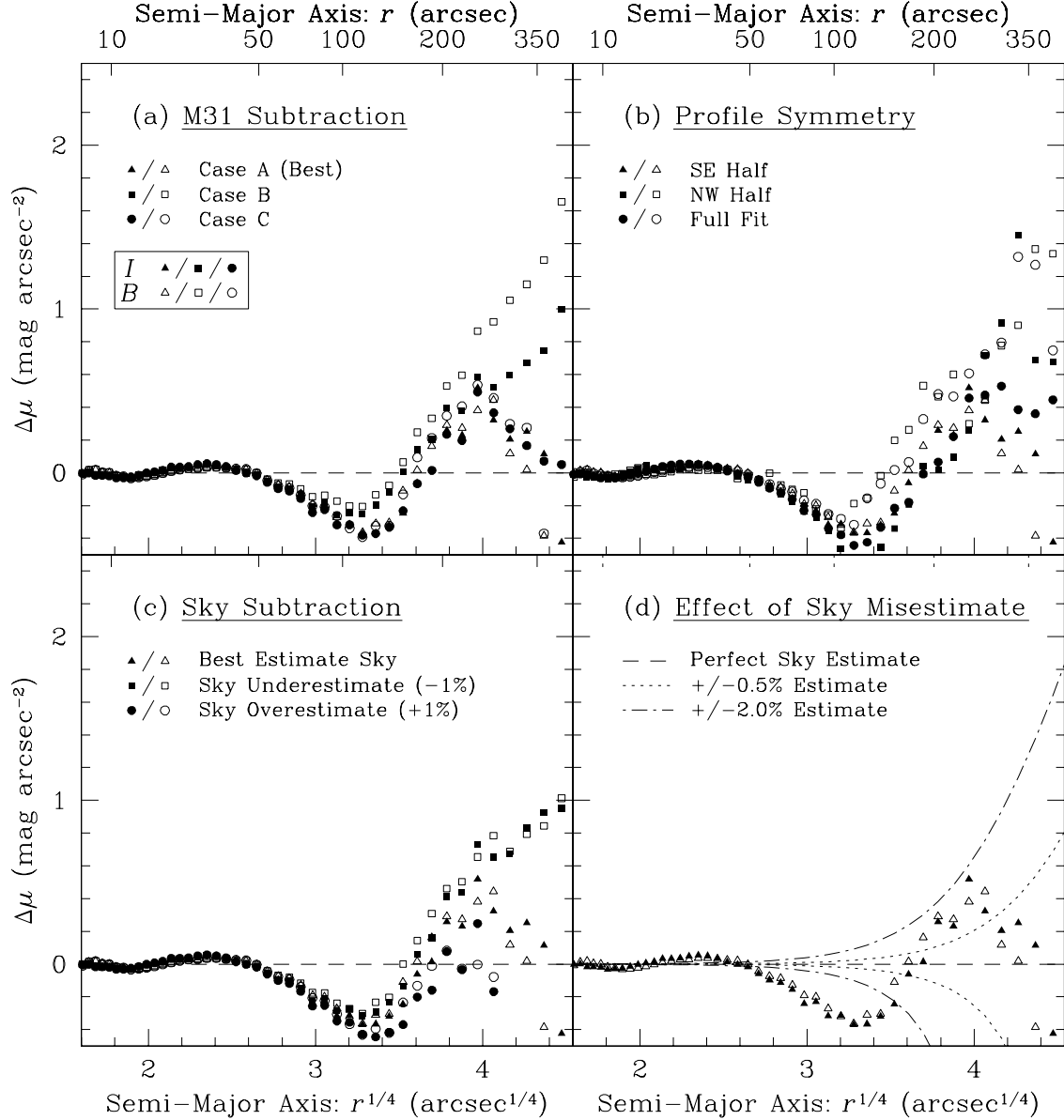
Fig. 8.— Surface brightness residuals $\Delta\mu$ — original minus "inner" fit $r^{1/4}$ law — for M32 in B (*open symbols*) and I bands (*filled symbols*). Various tests of the robustness of M32's surface brightness profile are illustrated. (*a*) Different degrees of removal of M31 disk light: best subtraction (Case A; *triangles*), extreme under-subtraction (Case B; *squares*), and extreme over-subtraction (Case C; *squares*) in the general vicinity of M32. (*b*) Ellipse fits to different parts of M32: SE half of major axis towards M31's outer disk (*triangles*), NW half of major axis towards M31's inner disk (*squares*), and the entire galaxy (*circles*). (*c*) Different degrees of removal of a constant sky background: best subtraction (*triangles*), 1% under-subtraction (*squares*), and 1% over-subtraction (*squares*). (*d*) Expected effect of sky subtraction error on a galaxy with an intrinsic $r^{1/4}$ law brightness profile: perfect sky estimate (*dashed*), $\pm 0.5\%$ error (*dotted*), and $\pm 2\%$ error (*dot-dashed*). The best estimate of M32's residual profile (*triangles*) shows a distinct shape that cannot simply be the result of sky subtraction error on a galaxy with a $r^{1/4}$ law profile. The consistency of the M32 residuals across B and I bands for these various tests (*a–c*) for $r \lesssim 250''$ demonstrates the robustness of the surface photometry and the significance of the depletion zone
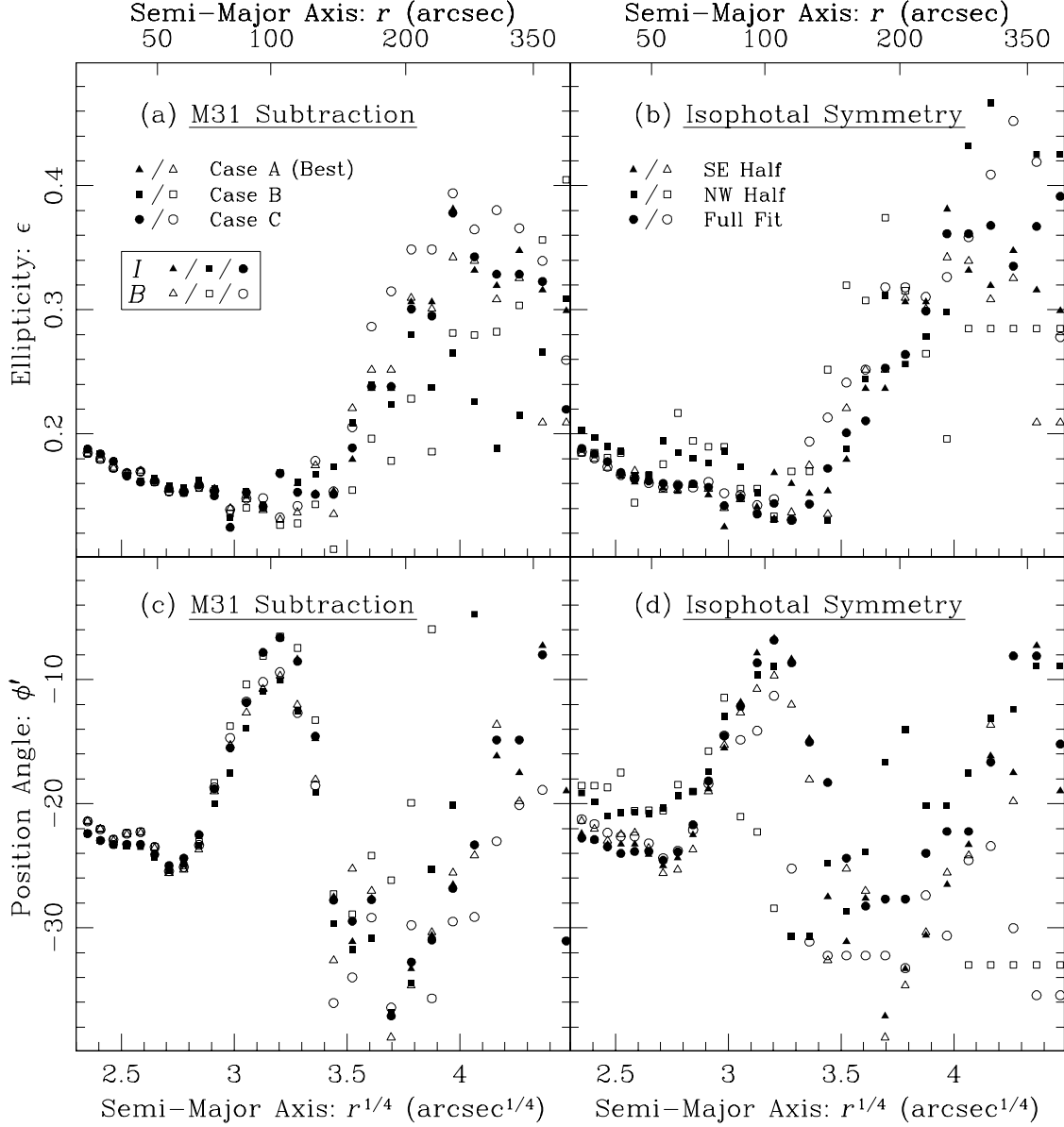
Fig. 9.— Tests of the robustness of the isophotal shape/orientation parameters.   (*a, b*) Same as Figure 8(*a, b*) respectively for isophotal ellipticity ϵ.   (*c, d*) Same as Figure 8(*a, b*) respectively for isophotal position angle ϕ'. The ϵ and ϕ' profiles are consistent between B and I bands, insensitive to details of M31 disk light subtraction, and symmetric about M32's center. The only exception is the B-band ϕ' profile derived from the fit to the NW half of M32 (indicated in (d) with *open squares*) that is likely affected by M31 disk residual features.
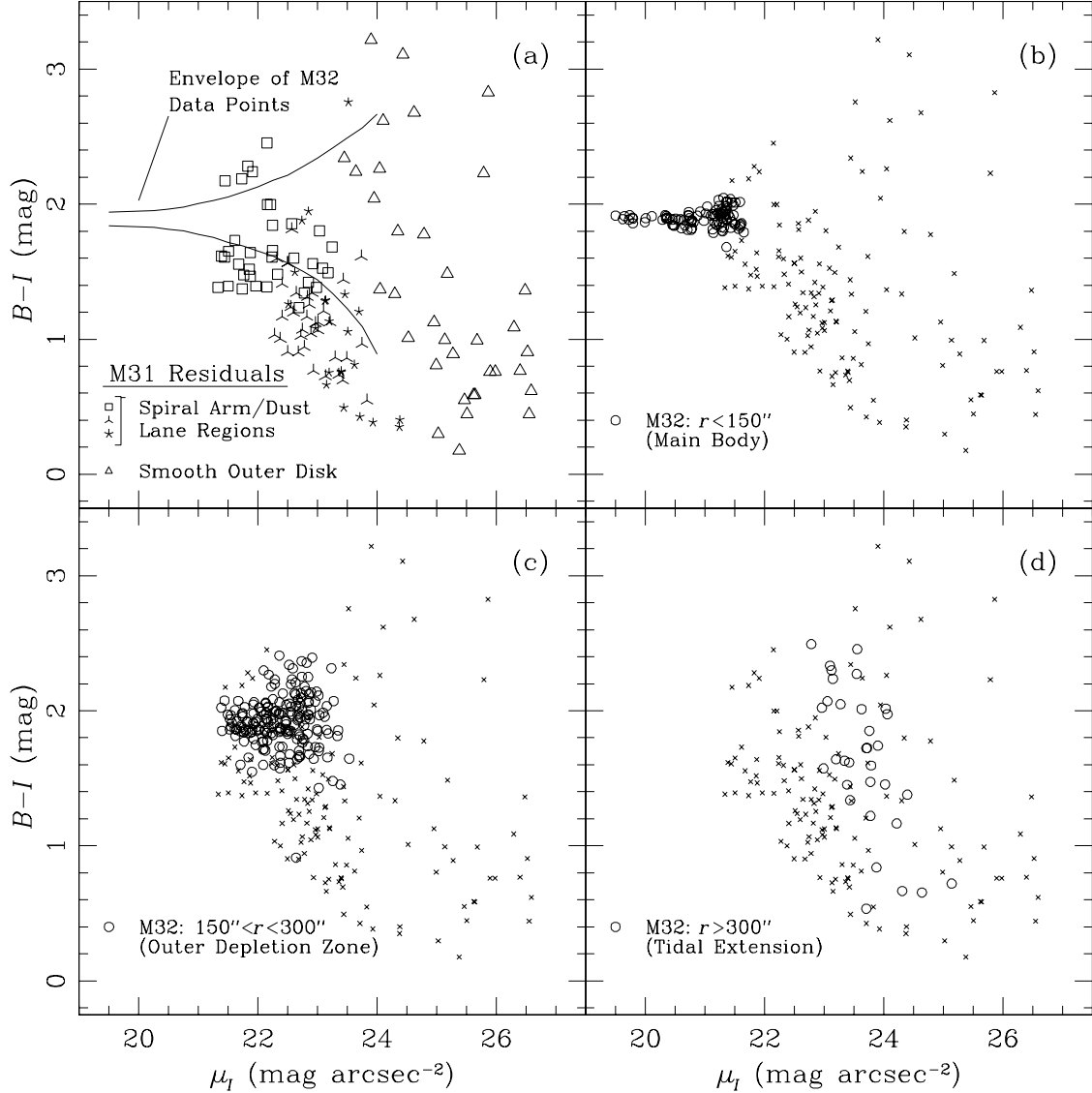
Fig. 10.— Color versus surface brightness for the area enclosed by the elliptical isophotes fit to M32 and areas in the surrounding field. (*a*) Regions sampling M31 disk residual features in four areas well away from M32 (*stars, crosses, squares, triangles*) plotted against the approximate envelope of measured data points within the area of the M32 isophotes (*solid lines*). Measurements are made for various subregions within the M32 isophotal ellipses (*open circles*) that are then grouped into radial bins: (*b*) $r < 150''$, (*c*) $150'' < r < 300''$, and (*d*) $r > 300''$. Surrounding field measurements are shown as *small crosses* [same data points as in (*a*)]. The various M32 subregions from the bright center to the faint outer isophotes ($r \sim 300''$) form a well-defined horizontal locus, in contrast to M31 residual disk features in the wider field which tend to be bluer. This suggests that the isophotes in the range $150'' < r < 300''$ (over which tidal signatures are observed) are indeed associated with M32 with relatively little contamination by residual M31 disk features.
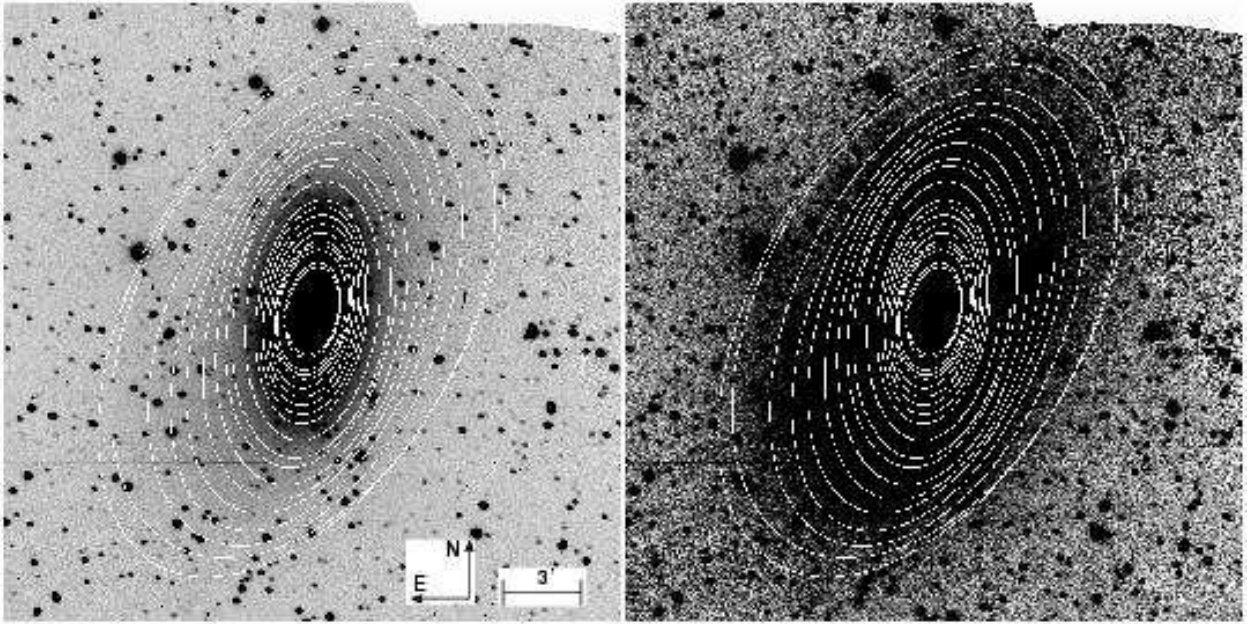
Fig. 11.— Grayscale representations of B-band images of NGC 205 covering $24' \times 24'$ at low (*left*) and high (*right*) contrast, with M31's disk light subtracted. Best-fit elliptical isophotes in the semi-major axis range $140'' < r < 660''$ highlight the region in which pronounced isophote twisting is observed.
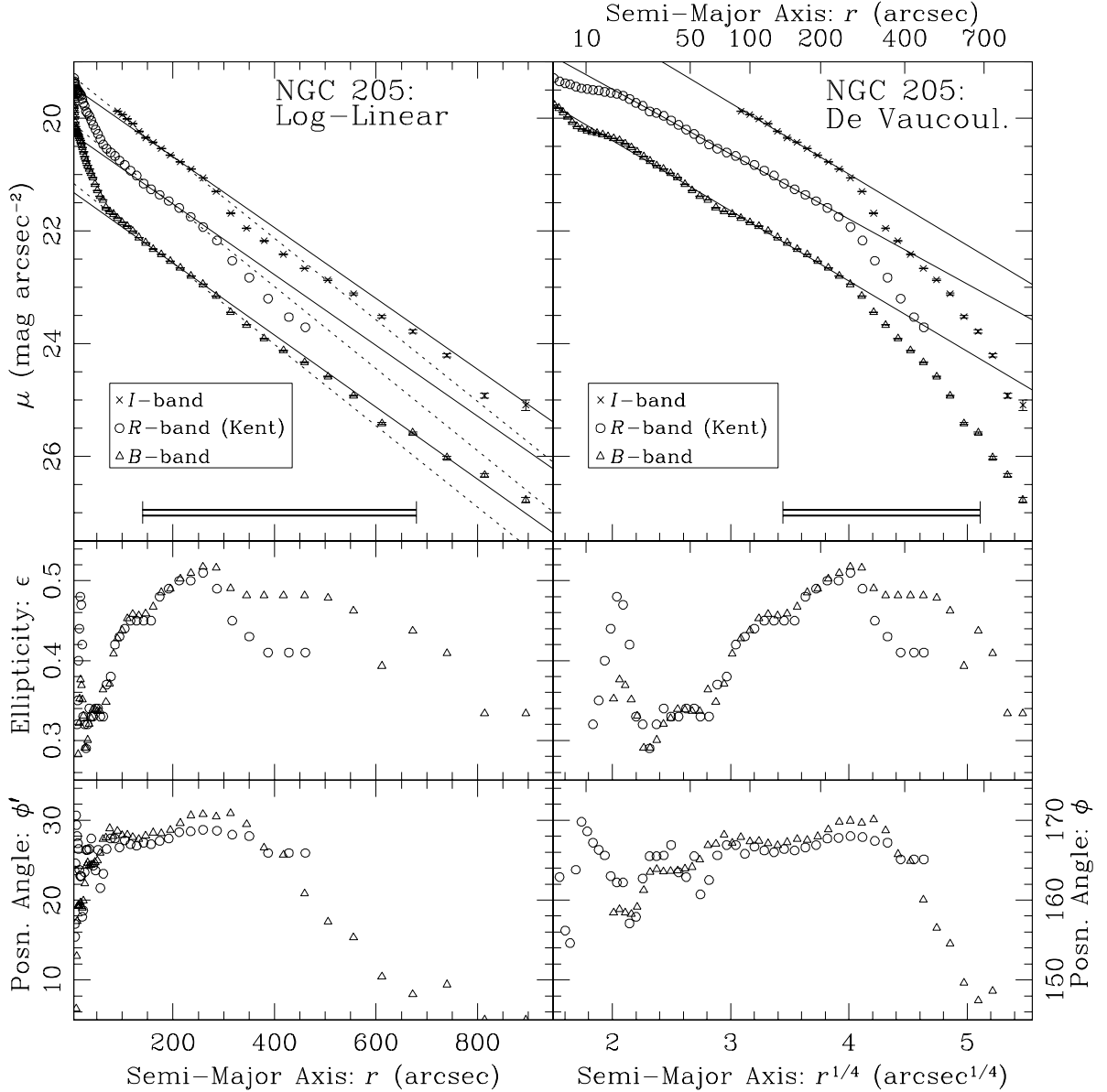
Fig. 12.— *Top to bottom*: Surface brightness μ, ellipticity ϵ, and position angle ϕ' (measured relative to the NGC 205→M31 vector, positive in the direction N→E [$|\phi'_{\text{NGC 205}}| = |\phi_{\text{NGC 205}} - 132.9°|$]) of NGC 205's isophotes versus semi-major axis length in log-linear (*left*) and de Vaucouleurs (*right*) coordinates in B (*triangles*), R (*circles*; Kent 1987), and I (*crosses*; only μ data due to partial coverage of the I-band images). An exponential law with $r^{\text{exp}}_{B,R,I} \sim 170''$ fits the profile over the range $150'' < r < 250''$ (*solid lines*), while one with $r^{\text{exp}}_{B,R,I} \sim 150''$ fits over the range $75'' < r < 250''$ (*dashed lines*). Note the subtle *downward* break at $r \sim 300''$, coincident with a sharp change in the ϵ and ϕ' profiles. The double bars marking the range $140'' < r < 680''$ in the μ plot show the region covered by the contours in Figure 11.
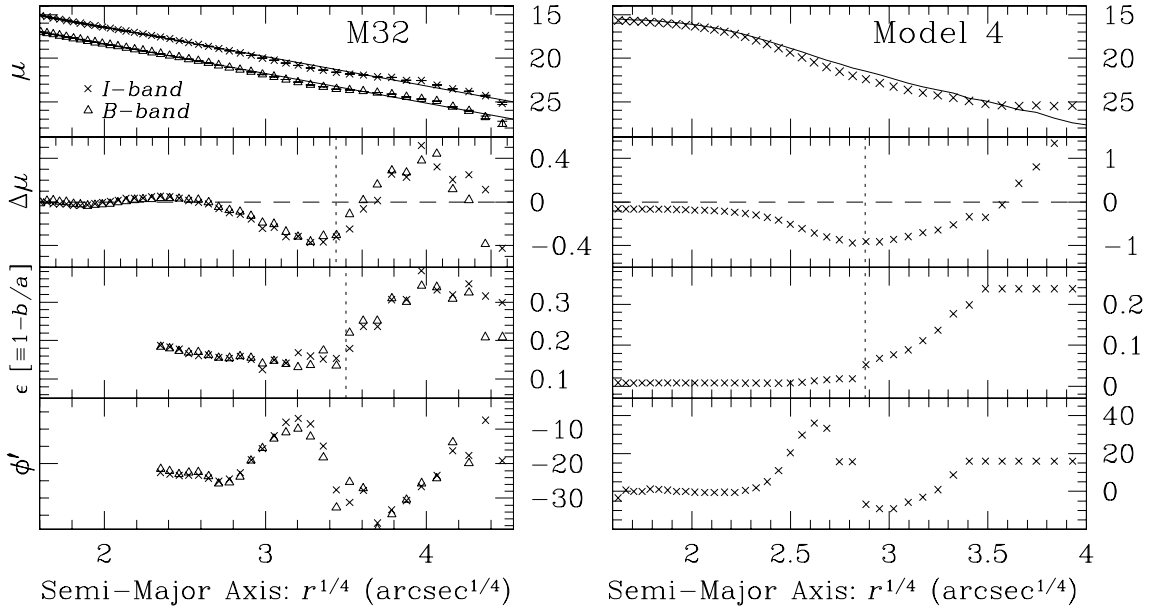
Fig. 13.— *Top to bottom*: Surface brightness μ, surface brightness residual $\Delta\mu$, ellipticity ϵ, and position angle ϕ' (measured relative to the satellite→parent vector) profiles of M32 (*left*) in B (*triangles*) and I (*crosses*) bands and of a snapshot of a simulated satellite with high orbital eccentricity ($e = 0.88$) at an orbital phase preceding apocenter (*right*). The residual $\Delta\mu$ is measured relative to the "inner" $r^{1/4}$ law fit for M32 (Fig. 6) and relative to the initial profile for the simulated satellite (*solid lines in top panels*). The locations of r_{break} and r_{distort} are shown as dotted vertical lines in the $\Delta\mu$ and ϵ plots, respectively. The two sets of profiles show similar features, including the unusual triple break in the ϕ' profile, indicating that M32 is likely to be on an eccentric orbit approaching apocenter.
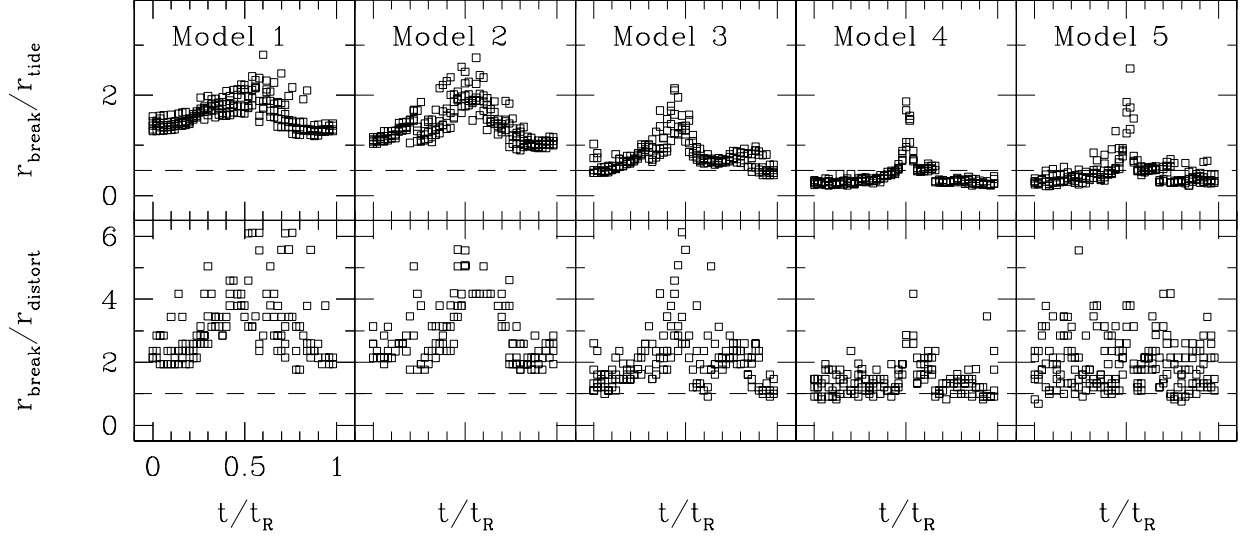
Fig. 14.— The ratios $r_{\rm break}/r_{\rm tide}$ (*upper*) and $r_{\rm break}/r_{\rm distort}$ (*lower*) plotted versus orbital phase as measured in numerical simulations of tidally disrupted satellites. Satellite orbital eccentricities are $e = 0.10/0.29/0.67/0.88$ for Model 1 (nearly circular) through Model 4 (highly elongated), respectively. Model 5 follows the same orbit as Model 4, but adopts a shallower initial density profile for the satellite than Models 1–4. The measured ratios for M32 (*dashed lines*) indicate that it is likely to be on an eccentric orbit ($e_{\rm M32} \geq 0.5$).
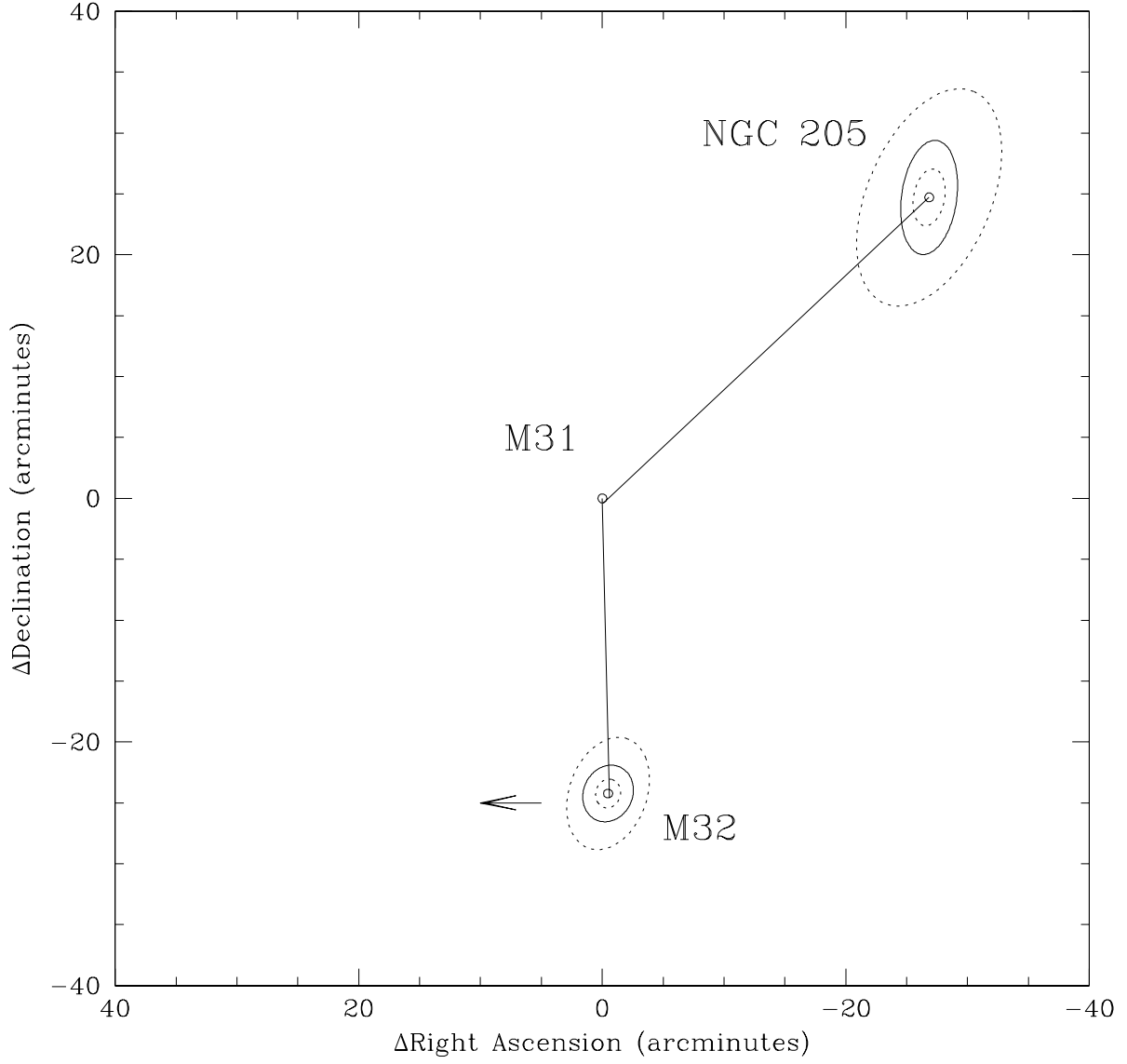
Fig. 15.— Orientation of ellipses fit to M32 and NGC 205 relative to M31. The solid ellipse is at r_{break} and the dotted ellipses are at 0.5 and 2 r_{break}. North is up and east is left as in Figures 3 and 11. The arrow indicates the probable direction of M32's projected orbit (see §6.3).
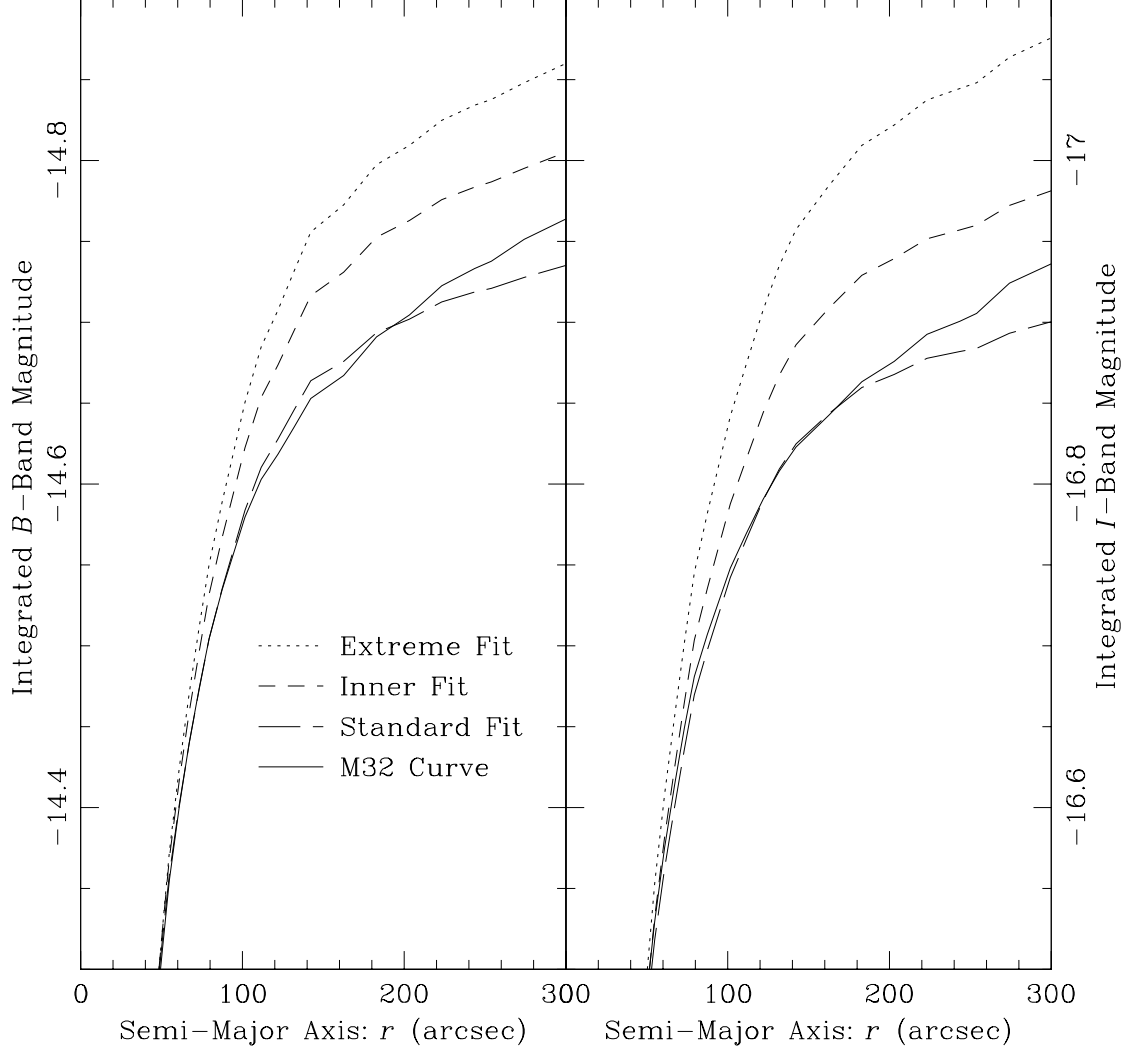
Fig. 16.— Absolute magnitude, based on integrated light within an isophote, as a function of isophotal radius ("curve of growth") for M32 in B (*left*) and I (*right*) bands. The growth curve for the measured M32 profile (*solid line*) is shown in contrast to curves based on integration of the standard, inner and extreme-inner (*long dashed, short dashed, dotted lines*) $r^{1/4}$ law fits listed in Table 1. Adopting either the inner or extreme-inner fit as M32's intrinsic profile suggests that its luminosity (within the $r = 300''$ isophote) has evolved by $\Delta B \sim 0.05 - 0.10$ and $\Delta I \sim 0.05 - 0.15$.

Table 1.   M32 de Vacouleurs Profile Fit Parameters

Band	r_{inner} ($''$)	r_{outer} ($''$)	r_{eff} ($''$)	μ_{eff} (mag)	$\Delta\mu_{\text{eff}}$ (mag)	Comments
R	15	100	32.0	18.79	—	Kent (1987) Data
R	10	140	32.5	18.64	—	Kent (1987) Data
I	10	140	28.5	17.53	—	Standard Fit
B	10	140	28.5	19.43	—	Standard Fit
I	10	65	36.8	18.00	0.47	Inner Fit
B	10	65	36.4	19.90	0.47	Inner Fit
I	10	30	46.8	18.41	0.88	Extreme-Inner Fit
B	10	30	42.0	20.15	0.72	Extreme-Inner Fit

Table 2.   Observed Profile Parameters and Derived Quantities for M32 & NGC 205

Name	R_{proj}[a] (kpc)	r_{tide}[a] (kpc)	r_{break}[a] (kpc)	r_{distort}[a] (kpc)	$\epsilon(\text{break})$	$\phi'(\text{break})$	$rd\phi'/dr(r_{\text{break}})$	df/dt
M32	5.5	1.2	0.54	0.57	0.14	-25.24	12.60	0.38
NGC 205	8.3	1.0	1.07	—	0.52	-36.32	66.26	2.95

[a]Based on an assumed distance to M31, M32, and NGC 205 of 780 kpc